International Journal of Multiphase Flow 59 (2014) 24–43

Contents lists available at ScienceDirect

International Journal of Multiphase Flow

journal homepage: www.elsevier.com/locate/ijmulflow

Lattice Boltzmann simulations of drop deformation and breakup in shear flow

A.E. Komrakova [a,*], Orest Shardt [a], D. Eskin [b], J.J. Derksen [a]

[a] Chemical and Materials Engineering, University of Alberta, 7th Floor, ECERF, 9107 116 St., Edmonton, Alberta T6G 2V4, Canada
[b] Schlumberger DBR Technology Center, 9450 17 Ave. NW, Edmonton, Alberta T6N 1M9, Canada

ARTICLE INFO

Article history:
Received 28 May 2013
Received in revised form 29 August 2013
Accepted 9 October 2013
Available online 28 October 2013

Keywords:
Drop deformation and breakup
Lattice Boltzmann method
Binary liquid model
Peclet and Cahn numbers

ABSTRACT

The behavior of a single liquid drop suspended in another liquid and subjected to simple shear flow is studied numerically using a diffuse interface free energy lattice Boltzmann method. The system is fully defined by three physical, and two numerical dimensionless numbers: a Reynolds number Re, a capillary number Ca, the viscosity ratio λ, an interface-related Peclet number *Pe*, and the ratio of interface thickness and drop size (the Cahn number *Ch*). The influence of *Pe*, *Ch* and mesh resolution on accuracy and stability of the simulations is investigated. Drops of moderate resolution (radius less than 30 lattice units) require smaller interface thickness, while a thicker interface should be used for highly resolved drops. The Peclet number is controlled by the mobility coefficient Γ. Based on the results, the simulations are stable when Γ is in the range 1–15. In addition, the numerical tool is verified and validated in a wide range of physical conditions: $\mathrm{Re} = 0.0625 - 50, \lambda = 1, 2, 3$ and a capillary number range over which drops deform and break. Good agreement with literature data is observed.

1. Introduction

When drops of one liquid dispersed in another immiscible liquid are subjected to shear flow, they start to deform. If the local shear rate is sufficiently large, the drops might break up into fragments. The study of the dynamics and mechanisms of drop breakup in shear flow is of fundamental importance in dispersion science and mixing processes. Experimental and theoretical investigations in this area focus on analyzing how strong the flow should be to break the drop, what the necessary energy input is to create the required intensity of the flow, and what the resulting drop size distribution (DSD) and rheology of the mixture are (Rallison, 1984). The results obtained in such studies can be applied to the formation of dispersions and emulsions and in particular the design of efficient mixing devices (Rallison, 1984). The application of shear to a premixed emulsion of various drop sizes is a technique for the production of monodisperse droplets (Cristini and Renardy, 2006).

Stirred tank reactors are widely used to obtain liquid–liquid dispersions under turbulent flow conditions. Turbulent flows contain a spectrum of eddies of different size, intensity, and lifetime (Pope, 2000). Drops continuously interact with these eddies. Large eddies convect small droplets with little deformation. When the droplet size is comparable to the eddy size, the drop can be significantly deformed and subsequently broken. Even though the randomness of turbulent flow implies complex drop/eddy interactions, simpler interactions can be identified. For example, a drop in a simple shear flow represents drop interaction with two co-rotating eddies in turbulent flow. The investigation of drop behavior in simple shear flow is more reproducible both experimentally and numerically than behavior in turbulent flow. The results obtained in such studies are helpful when it comes to engineering applications. To demonstrate that, consider a water-based turbulently agitated liquid–liquid system. Let the size of the drop be comparable to the Kolmogorov length scale. The kinematic viscosity of the continuous phase is of the order of $\nu = 10^{-6}$ m^2/s. The local energy dissipation rate in the impeller region (Davies, 1987) may be up to $\epsilon = 100$ W/kg. Based on these parameters the Kolmogorov time scale is $\tau_K = \sqrt{\nu/\epsilon} = 10^{-4}$ s. Suppose the resulting distribution of drop radii is in the range a = (1–100) μm. Assume that turbulent eddies interacting with the drop create a shear rate of the order of $\dot{\gamma} = 1/\tau_K$. Then the range of drop Reynolds number defined as $\mathrm{Re} = \dot{\gamma}a^2/\nu$ is from 0.01 to 100. This implies that even in fully-developed turbulence, drops experience interactions with eddies at low to moderate Reynolds numbers. Therefore, a study of binary systems in simple shear flow has direct relevance to complex turbulently flowing systems. One can, for example, check if the local energy dissipation rate is high enough to break drops of certain sizes and eventually obtain liquid–liquid dispersions with desired characteristics.

Starting with experiments performed by Taylor (1932, 1934), a wide range of studies has been carried out on drop deformation

* Corresponding author.
E-mail address: komrakov@ualberta.ca (A.E. Komrakova).

0301-9322/$ - see front matter © 2013 Elsevier Ltd. All rights reserved.
http://dx.doi.org/10.1016/j.ijmultiphaseflow.2013.10.009

and breakup. These studies have been reviewed by Rallison (1984), Stone (1994), and Cristini and Renardy (2006). The "retractive end pinching" breakup mechanism was outlined by Bentley and Leal (1986). Marks (1998) investigated "elongative end pinching" by applying a strong shear to a single drop. Recent experiments have been performed by Zhao (2007) where a dilute emulsion was subjected to a simple shear flow. A map of drop breakup mechanisms in simple shear flow as a function of viscosity ratio and capillary number was presented.

A viscous drop under shear flow has also been intensively investigated by means of numerical simulations. Most of the numerical studies have been performed with the boundary integral method (Kennedy et al., 1994; Kwak and Pozrikidis, 1998; Cristini et al., 2003; Janssen and Anderson, 2007). The method has been successfully applied for drop deformation studies. However, the implementation of the boundary integral method for drop breakup and coalescence poses a major obstacle because it is very difficult to handle merging and folding interfaces: the interface points should be reconstructed, which requires significant logical programming and results in computational overhead (Li et al., 2000). The mathematical implication of the boundary integral method such as singularity of the free-space Green's kernels is discussed by Pozrikidis (1992). A way to overcome this issue is suggested by Bazhlekov et al. (2004): a higher accuracy in the vicinity of the singular point is gained, however, the performance is about an order of magnitude slower compared to a standard surface integration. An alternative numerical technique widely used to investigate drop breakup is the volume-of-fluid (VOF) method. Numerical simulation of breakup of a viscous drop in simple shear flow was carried out by Li et al. (2000). The same technique has been applied by Renardy and Cristini (2001b), Renardy et al. (2002), Khismatullin et al. (2003), and Cristini and Renardy (2006). The topological changes of the interface are treated more naturally compared to the boundary integral method. The VOF method has been generalized to three-dimensional cases. However, the reconstruction of the interface requires significant computational effort that increases with the number of drops involved.

A droplet in a quiescent fluid was investigated by Van der Sman and van der Graaf (2008) using a free energy lattice Boltzmann model (LBM). The authors further analyzed the numerical criteria for a correct description of emulsions and applied the model to study drop deformation and breakup. All simulated cases were two-dimensional.

Three-dimensional numerical simulations of the classical Taylor experiment on droplet deformation in a simple shear flow have been performed by Xi and Duncan (1999). The authors applied the lattice Boltzmann method in conjunction with the interface force model of Shan and Chen (1993). Good agreement with theoretical predictions was demonstrated for small deformations. The ability of the method to capture larger deformations and breakup events was also shown.

In the present study, the free energy lattice Boltzmann method originally proposed by Swift et al. (1996) is adopted to perform three-dimensional simulations of a single liquid drop suspended in another liquid under simple shear flow. The goal of the study is to check the capability of the method to capture the physics of drop deformation and breakup in a wide range of flow conditions: starting from near Stokes flow up to drop Reynolds numbers of 50 where inertia plays a significant role. Also the ability of the method to handle liquids with different viscosities is tested.

Diffuse interface numerical techniques require an explicit specification of the interface thickness which essentially is a numerical artifact. It is necessary to examine how this impacts the simulations, what parameters determine this additional degree of freedom, and what values of these parameters should be set for physically realistic results. In addition, it is important to outline the resolution that is sufficient to capture the physics of drop breakup while keeping a reasonable simulation time. To validate the numerical approach, its results are compared to existing experimental results and findings of numerical simulations using other methods. The present study can be considered as a development towards a numerical tool to investigate the behavior of drops in shear flow and as a verification and validation step for further applications in more complex flows. For instance, the developed code would be extended to perform Direct Numerical Simulations (DNS) of turbulent dispersion formation with hundreds of breaking and merging droplets.

The rest of the paper is organized as follows. The problem statement is outlined in Section 2. Section 3 contains the details of the numerical technique. The results of simulations are presented in Section 4. First, the choice of the numerical parameters that determine drop behavior in shear flow is discussed in Section 4.1, with additional details in Appendix A. Drop deformation and breakup in Stokes flow is presented in Section 4.2, the influence of inertia on drop deformation is shown in Section 4.3 and Section 4.4 presents the joint influence of viscosity ratio and inertia on drop deformation and breakup scenarios. Finally, conclusions are drawn in Section 5.

2. Problem statement

A liquid drop of dynamic viscosity μ_d is suspended in another liquid of viscosity μ_c. The ratio of drop viscosity to surrounding liquid viscosity is denoted as $\lambda = \mu_d/\mu_c$. The interfacial tension between the liquids is σ. The liquids are of equal density ρ. At time $t = 0$, the drop is a sphere with radius a. The entire system undergoes simple shear flow between two parallel plates located a distance H apart (Fig. 1). The two plates translate in opposite directions with velocity u_w so that the shear rate is $\dot{\gamma} = 2u_w/H$.

Drop behavior in simple shear flow is determined by three dimensionless numbers which are the Reynolds number Re, the capillary number Ca, and the viscosity ratio λ:

$$\mathrm{Re} = \frac{\dot{\gamma}a^2}{\nu} \quad \mathrm{Ca} = \frac{a\dot{\gamma}\mu_c}{\sigma} \quad \lambda = \frac{\mu_d}{\mu_c} \tag{1}$$

In the case of vanishingly small Re (Stokes flow) only viscous and capillary forces determine the drop behavior. Being deformed under shear flow, the drop inclines in the direction of the flow, away from the axis of elongation which is at 45° to the flow direction (Khismatullin et al., 2003). It was shown by Khismatullin et al. (2003) and is demonstrated later in this paper that the addition of inertia changes the drop deformation and also the breakup process. The range of Reynolds numbers considered here is from 0.0625 to 50.

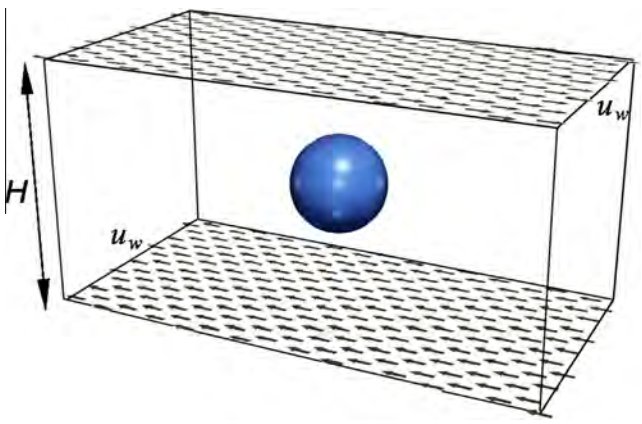

Fig. 1. Single drop under simple shear flow.

The ratio of viscous and capillary forces is determined by the capillary number. For each viscosity ratio λ there is a critical capillary number, Ca_c, above which the drop eventually breaks. For capillary numbers below the critical value, a steady drop shape exists. When the drop is sheared in the Stokes flow regime at $Ca \sim Ca_c$ it breaks up by the "end pinching" mechanism into daughter drops separated by smaller satellite and subsatellite droplets (Marks, 1998; Zhao, 2007). In this study, simulations close to Stokes flow conditions are performed for capillary numbers in the range of 0.1–0.42. This range of Ca includes drop deformation and breakup.

Finally, drop deformation and breakup depends on the viscosity ratio. When the drop is very viscous ($\lambda \gg 1$), the rate of elongation in the drop is small compared to the rate of circulation in the drop, and the drop cannot break (Cristini and Renardy, 2006). The critical viscosity ratio λ_c beyond which the drop does not break is around 3.0 for Stokes flow (Khismatullin et al., 2003; Cristini and Renardy, 2006). The critical viscosity ratio increases with increasing Reynolds number (Khismatullin et al., 2003). The viscosity ratios λ considered in this paper are 1, 2, and 3.

3. Numerical method

In the present study, a diffuse interface method is used to simulate the behavior of a drop in shear flow. In diffuse interface (or phase field) methods (Jacqmin, 1999; Yue et al., 2004; Ding et al., 2007; Magaletti et al., 2013) the sharp interface between fluids is represented by a thin transition region with finite thickness where fluids may mix. At any given time, the state of the system is described by the order parameter of the phase field ϕ which is the relative concentration of the two components (Cahn and Hilliard, 1958; Penrose and Fife, 1990; Badalassi et al., 2003). To simulate the fluid dynamics of a binary mixture of fluids, the continuity and momentum equations are used in conjunction with the convection–diffusion equation for the order parameter proposed by Cahn and Hilliard (1958, 1959). Thus, the evolution of density, velocity and order parameter are governed by the continuity, momentum, and convection–diffusion equations (De Groot et al., 1984; Swift et al., 1996; Kendon et al., 2001), respectively:

$$\partial_t \rho + \partial_\alpha(\rho u_\alpha) = 0 \tag{2a}$$

$$\partial_t(\rho u_\alpha) + \partial_\beta(\rho u_\alpha u_\beta) = -\partial_\beta P^{th}_{\alpha\beta} + \partial_\beta \nu\left(\rho\partial_\alpha u_\beta + \rho\partial_\beta u_\alpha\right) \tag{2b}$$

$$\partial_t \phi + \partial_\alpha(\phi u_\alpha) = M\partial^2_{\beta\beta}\mu \tag{2c}$$

where ρ and ν are the density and the kinematic viscosity of the mixture, respectively. Here $P^{th}_{\alpha\beta}$ is the 'thermodynamic' pressure tensor. It contains two parts (Kendon et al., 2001): an isotropic contribution $P\delta_{\alpha\beta}$ that represents the ideal gas pressure and the 'chemical' pressure tensor $P^{chem}_{\alpha\beta}$. The chemical potential in Eq. (2c) is: $\mu(\phi) = A\phi - A\phi^3 - \kappa\partial^2_{\alpha\alpha}\phi$. Here, $A < 0$ is a parameter of the free energy model; κ is a parameter related to the surface tension and interface thickness.

Swift et al. (1996) developed a lattice Boltzmann approach, known as the free energy model, to solve the system (2). Exactly this method is adopted in the present study. Two particle distribution functions are utilized: one function $f(\mathbf{r}, t)$ is used to solve the continuity (2a) and Navier–Stokes (2b) equations and the second one $g(\mathbf{r}, t)$ is used for the convection–diffusion Eq. (2c). The distribution functions evolve by a time step Δt. All simulations have been performed using a single relaxation time collision operator (Bhatnagar–Gross–Krook (BGK) model (Bhatnagar et al., 1954)). The discrete lattice Boltzmann equations have the following form:

$$\begin{aligned} f_q(r_\alpha + c_{\alpha q}\Delta t, t + \Delta t) - f_q(r_\alpha, t) &= -\frac{f_q - f_q^{eq}}{\tau_f} \\ g_q(r_\alpha + c_{\alpha q}\Delta t, t + \Delta t) - g_q(r_\alpha, t) &= -\frac{g_q - g_q^{eq}}{\tau_g} \end{aligned} \tag{3}$$

where the index q stands for the number of the discrete velocity directions; the index α stands for the Cartesian directions x, y and z; f_q^{eq}, g_q^{eq} are discretized Maxwell–Boltzmann distributions (or equilibrium distributions); $c_{\alpha q}$ denotes the discrete velocity set and τ_f, τ_g are dimensionless relaxation parameters. The D3Q19 lattice is adopted here where $Q = 19$ is the number of velocity directions. In this lattice arrangement, each site communicates with its six nearest and twelve diagonal neighbors. The lattice Boltzmann method operates in dimensionless lattice units (lattice space, time step, and lattice density for the length, time and density units, respectively). For the method described here, only uniform cubic lattices can be used; the mesh step Δx is taken as unity, as is the time step Δt. The discrete velocity set is defined as follows:

$$\begin{pmatrix} c_x \\ c_y \\ c_z \end{pmatrix} = \begin{bmatrix} 0 & c & -c & 0 & 0 & 0 & 0 & c & -c & c & -c & 0 & 0 & 0 & 0 & c & -c & c & -c \\ 0 & 0 & 0 & c & -c & 0 & 0 & c & c & -c & -c & c & -c & c & -c & 0 & 0 & 0 & 0 \\ 0 & 0 & 0 & 0 & 0 & c & -c & 0 & 0 & 0 & 0 & c & c & -c & -c & c & c & -c & -c \end{bmatrix}$$

where $c = \Delta x/\Delta t$ is the lattice speed.

The particle distribution functions are defined such that the following summations over all directions q at each single lattice point give the local density of the fluid, the local fluid momentum and the local order parameter, respectively:

$$\sum_q f_q = \rho \quad \sum_q c_{\alpha q} f_q = \rho u_\alpha \quad \sum_q g_q = \phi \tag{4}$$

The equilibrium distributions (Kusumaatmaja, 2008) f_q^{eq}, g_q^{eq} for populations $1 \leqslant q \leqslant (Q-1)$ are calculated using the following relations:

$$\begin{aligned} f_q^{eq} = {} & \frac{w_q}{c^2}\left(p_0 - \kappa\phi(\partial^2_{xx}\phi + \partial^2_{yy}\phi + \partial^2_{zz}\phi) + c_{\alpha q}\rho u_\alpha \right. \\ & \left. + \frac{3}{2c^2}\left[c_{\alpha q}c_{\beta q} - \frac{c^2}{3}\delta_{\alpha\beta}\right]\rho u_\alpha u_\beta\right) \\ & + \frac{\kappa}{c^2}\left(w_q^{xx}\partial_x\phi\partial_x\phi + w_q^{yy}\partial_y\phi\partial_y\phi + w_q^{zz}\partial_z\phi\partial_z\phi + w_q^{xy}\partial_x\phi\partial_y\phi \right. \\ & \left. + w_q^{xz}\partial_x\phi\partial_z\phi + w_q^{yz}\partial_y\phi\partial_z\phi\right) \\ g_q^{eq} = {} & \frac{w_q}{c^2}\left(\Gamma\mu + c_{\alpha q}\rho u_\alpha + \frac{3}{2c^2}\left[c_{\alpha q}c_{\beta q} - \frac{c^2}{3}\delta_{\alpha\beta}\right]\phi u_\alpha u_\beta\right) \end{aligned} \tag{5}$$

while the distributions for $q = 0$ are given by:

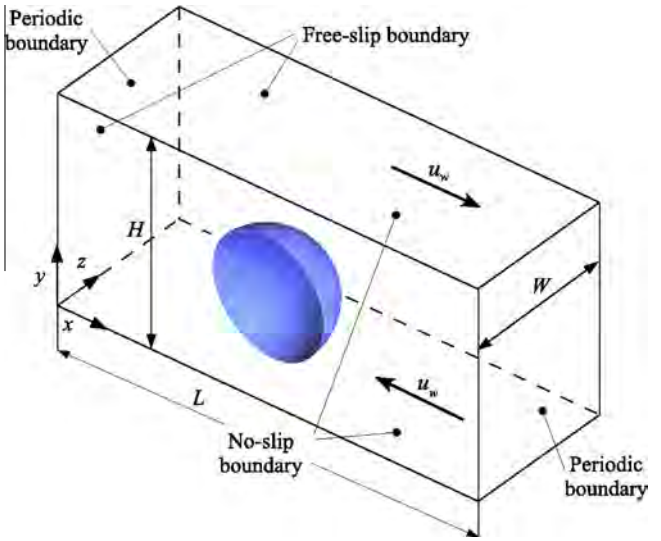

Fig. 2. Simulation domain with boundary conditions: $x = 0$ and $x = L$ are periodic boundaries; $y = 0$ and $y = H$ are no-slip walls moving with constant velocity u_w; $z = 0$ and $z = W$ are the symmetry planes. At $t = 0$ the drop has a spherical shape. Due to the symmetry of the problem only half of the drop has been simulated.

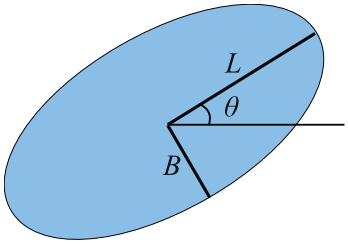

Fig. 3. Drop elongation L, deformation $D = (L-B)/(L+B)$ and orientation angle θ measurements.

Table 1
Wall proximity influence (H is a distance between the moving plates). Elongation L/a and orientation angle θ of a drop with undeformed radius $a = 20$ [lu] at $\mathrm{Ca} = 0.27, \mathrm{Re} = 1, \lambda = 1, Pe = 1$ and $Ch = 0.057$.

	$H = 4a$	$H = 8a$	$H = 16a$
L/a (LBM)	1.93	1.87	1.82
θ (LBM)	18.88	22.77	23.12
L/a (VOF) (Renardy and Cristini, 2001a)		1.8	
θ (VOF) (Renardy and Cristini, 2001a)		25	

$$f_0^{\mathrm{eq}} = \rho - \sum_{q=1}^{Q-1} f_q^{\mathrm{eq}} \quad g_0^{\mathrm{eq}} = \phi - \sum_{q=1}^{Q-1} g_q^{\mathrm{eq}} \tag{6}$$

And the weights (Kusumaatmaja, 2008) are:

$$\begin{aligned}
&w_{1-6} = \frac{1}{6}, \quad w_{7-18} = \frac{1}{12} \\
&w^{xx}_{1-2} = w^{yy}_{3-4} = w^{zz}_{5-6} = \frac{5}{12}, \quad w^{xx}_{3-6} = w^{yy}_{1-2,5-6} = w^{zz}_{1-4} = -\frac{1}{3} \\
&w^{xx}_{7-10} = w^{xx}_{15-18} = w^{yy}_{7-14} = w^{zz}_{11-18} = -\frac{1}{24} \\
&w^{xx}_{11-14} = w^{yy}_{15-18} = w^{zz}_{7-10} = \frac{1}{12} \\
&w^{xy}_{1-6} = w^{yz}_{1-6} = w^{zx}_{1-6} = 0, \quad w^{xy}_{7,10} = w^{yz}_{11,14} = w^{zx}_{15,18} = \frac{1}{4} \\
&w^{xy}_{8-9} = w^{yz}_{12-13} = w^{zx}_{16-17} = -\frac{1}{4}, \quad w^{xy}_{11-18} = w^{yz}_{7-10} = w^{zx}_{7-14} = 0
\end{aligned} \tag{7}$$

The bulk pressure in Eq. (5) is defined as $p_0 = c_s^2\rho + \frac{A}{2}\phi^2 - \frac{3A}{4}\phi^4$. Here $c_s^2 = 1/3$ is the speed of sound in lattice units.

The mobility M, the coefficient of mobility Γ and the relaxation parameter τ_g are connected by the following relation:

$$M = \Delta t \Gamma \left(\tau_g - \frac{1}{2}\right) \tag{8}$$

i.e. the parameter Γ determines the order parameter mobility M.

The liquids have different kinematic viscosity. To take this into account, the kinematic viscosity of the mixture v is set to be a function of the order parameter ϕ:

$$v(\phi) = v_c \frac{\phi_0 - \phi}{2\phi_0} + v_d \frac{\phi_0 + \phi}{2\phi_0} \tag{9}$$

where v_c and v_d are the kinematic viscosities of continuous and dispersed phases, respectively. The relaxation parameter for f_q is defined using the kinematic viscosity of the mixture:

$$\tau_f(\phi) = \frac{v(\phi)}{c_s^2 \Delta t} + \frac{1}{2} \tag{10}$$

For a planar interface, an analytical solution (Van der Sman and van der Graaf, 2008) gives the ϕ profile $\phi(x) = \phi_0 \tanh(x/\xi)$. Here, $\phi = \pm\phi_0 = \pm 1$ is the value of order parameter in the bulk phase at either side of the interface. The thickness of the diffuse interface ξ is equal to

$$\xi = \left(\frac{2\kappa}{-A}\right)^{1/2} \tag{11}$$

The surface tension σ follows from:

$$\sigma = \frac{4}{3}\kappa\frac{\phi_0^2}{\xi} \tag{12}$$

To determine the equilibrium distributions (5), the spatial gradients of ϕ have to be calculated. The stencils for gradients and Laplacian calculations adopted in this study are (Kusumaatmaja, 2008):

$$\partial_x = \frac{1}{12\Delta x}\left[\begin{pmatrix} 0 & 0 & 0 \\ -1 & 0 & 1 \\ 0 & 0 & 0 \end{pmatrix}, \begin{pmatrix} -1 & 0 & 1 \\ -2 & 0 & 2 \\ -1 & 0 & 1 \end{pmatrix}, \begin{pmatrix} 0 & 0 & 0 \\ -1 & 0 & 1 \\ 0 & 0 & 0 \end{pmatrix}\right] \tag{13}$$

$$\nabla^2 = \frac{1}{6\Delta x^2}\left[\begin{pmatrix} 0 & 1 & 0 \\ 1 & 2 & 1 \\ 0 & 1 & 0 \end{pmatrix}, \begin{pmatrix} 1 & 2 & 1 \\ 2 & -24 & 2 \\ 1 & 2 & 1 \end{pmatrix}, \begin{pmatrix} 0 & 1 & 0 \\ 1 & 2 & 1 \\ 0 & 1 & 0 \end{pmatrix}\right] \tag{14}$$

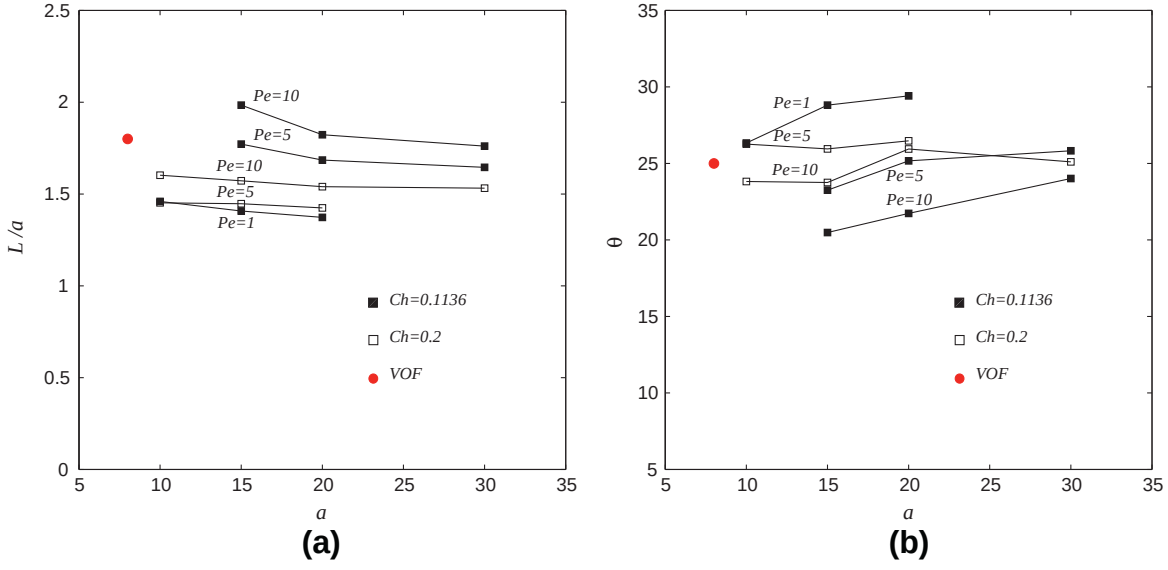

Fig. 4. Drop deformation results at $\mathrm{Re} = 1, \mathrm{Ca} = 0.27, \lambda = 1$ and different Pe and Ch numbers. The L/a ratio (a) and the orientation angle θ (b) as a function of drop radius.

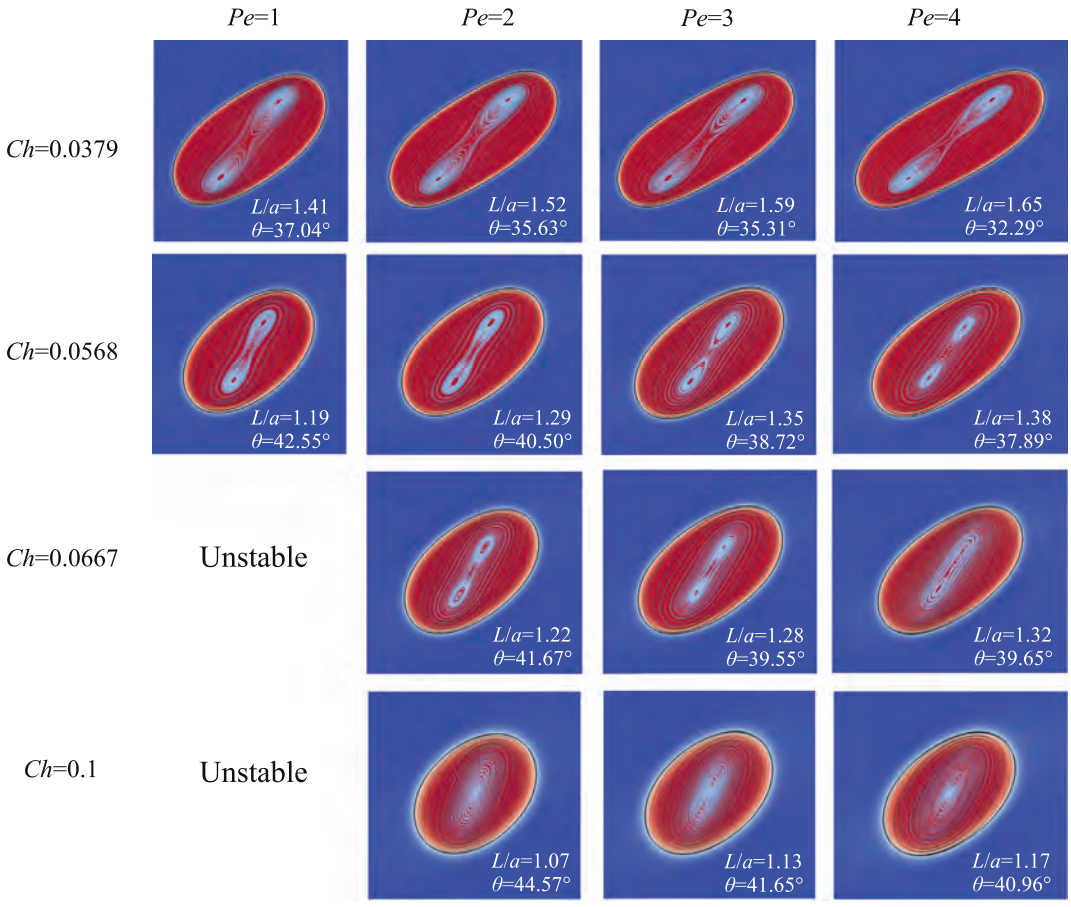

Fig. 5. Drop shape and streamlines at steady-state for drop with radius $a = 30$ [lu] at $\mathrm{Re} = 10, \mathrm{Ca} = 0.15, \lambda = 1$ and different *Pe* and *Ch* numbers.

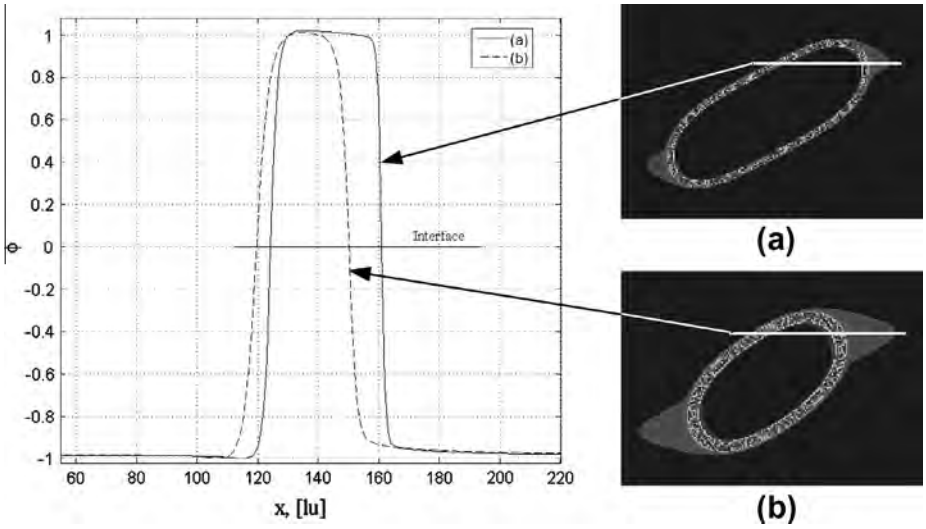

Fig. 6. Drop shape (ϕ field) at steady state. The drop radius is $a = 30$ [lu] and $Pe = 3$. (a) $\xi = 1.14$ [lu], $\Gamma = 4.3$; (b) $\xi = 2$ [lu], $\Gamma = 13.3$.

where the left, middle and right matrices show slices of the stencil when $z = \Delta x, 0$ and $-\Delta x$, respectively.

The discretized Eqs. (3) are solved in two steps:

$$\text{Collision step}: \quad f_q'(r_\alpha, t) = f_q(r_\alpha, t) - \frac{1}{\tau_f}[f_q - f_q^{\mathrm{eq}}]$$
$$g_q'(r_\alpha, t) = g_q(r_\alpha, t) - \frac{1}{\tau_g}[g_q - g_q^{\mathrm{eq}}] \qquad (15)$$

$$\text{Streaming step}: \quad f_q(r_\alpha + c_{\alpha q}\Delta t, t + \Delta t) = f_q'(r_\alpha, t)$$
$$g_q(r_\alpha + c_{\alpha q}\Delta t, t + \Delta t) = g_q'(r_\alpha, t) \qquad (16)$$

To complete the mathematical description, boundary conditions have to be specified. The simulation domain with boundary conditions is depicted in Fig. 2. The no-slip condition is imposed on the bottom $y = 0$ and top $y = H$ plates for the f_q distribution and a Dirichlet condition of $\phi = -\phi_0$ for the g_q distribution. The

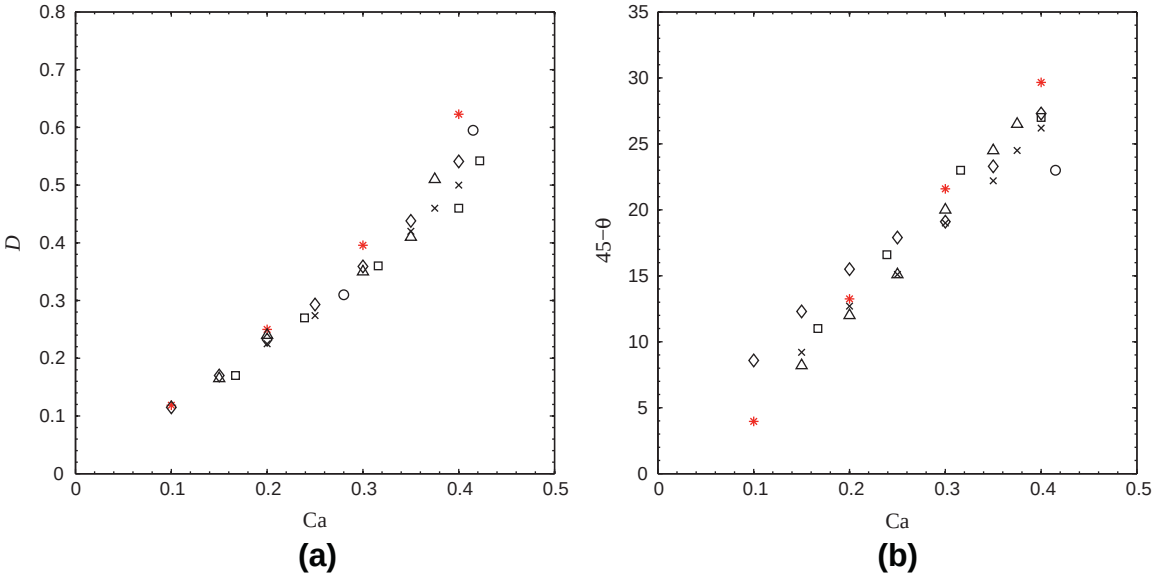

Fig. 7. Deformation (a) and orientation (b) of a drop in simple shear flow under near Stokes conditions. Present simulation results (at Re = 0.0625) with free energy LBM ✳; Previous results: ♢ VOF computations of Li et al. (2000); □ boundary integral method of Rallison (1981); × boundary integral method of Kwak and Pozrikidis (1998); △ boundary integral method of Kennedy et al. (1994); ○ experimental results by Mason and Bibette (1997).

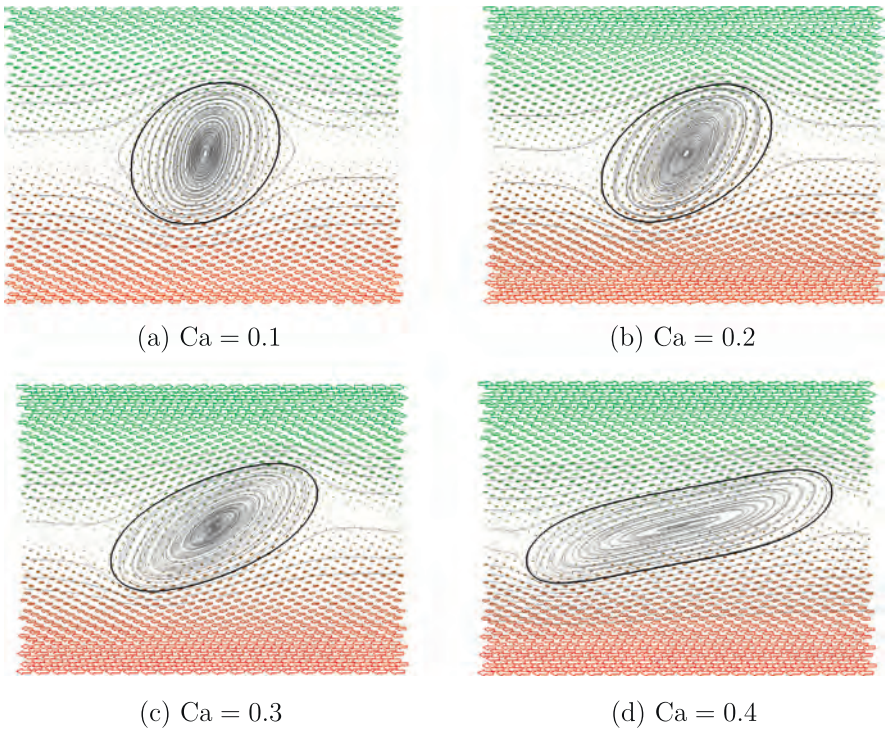

Fig. 8. Steady state drop shape (black curve stands for the interface), streamlines and velocity fields (x–y plane at $z = 0$). Stokes flow (Re = 0.0625), $\lambda = 1$.

constant velocities of the walls are applied on those planes using the procedure proposed by Mussa et al. (2009). The rest of the boundary conditions apply to both f_q and g_q. Periodic conditions are imposed on the $x = 0$ and $x = L$ planes. Because of the symmetry of the problem, only half of the drop has been considered. Such consideration requires symmetry conditions (Ahmed and Hecht, 2009) of the side planes $z = 0$ and $z = W$. The initial condition at time $t = 0$ is that the drop has a spherical shape and the velocity field is zero throughout the domain.

4. Simulations of a single drop under simple shear flow

A computer code for three-dimensional simulations is developed using Fortran 90 in both serial and parallel versions. The parallel code uses domain decomposition and MPI (Message Passing Interface). The simulation domain is decomposed into slabs in the x direction, one for each CPU. The number of CPUs used depends on the domain size, starting from one for low resolution drops and up to eight CPUs for the highest resolution drops.

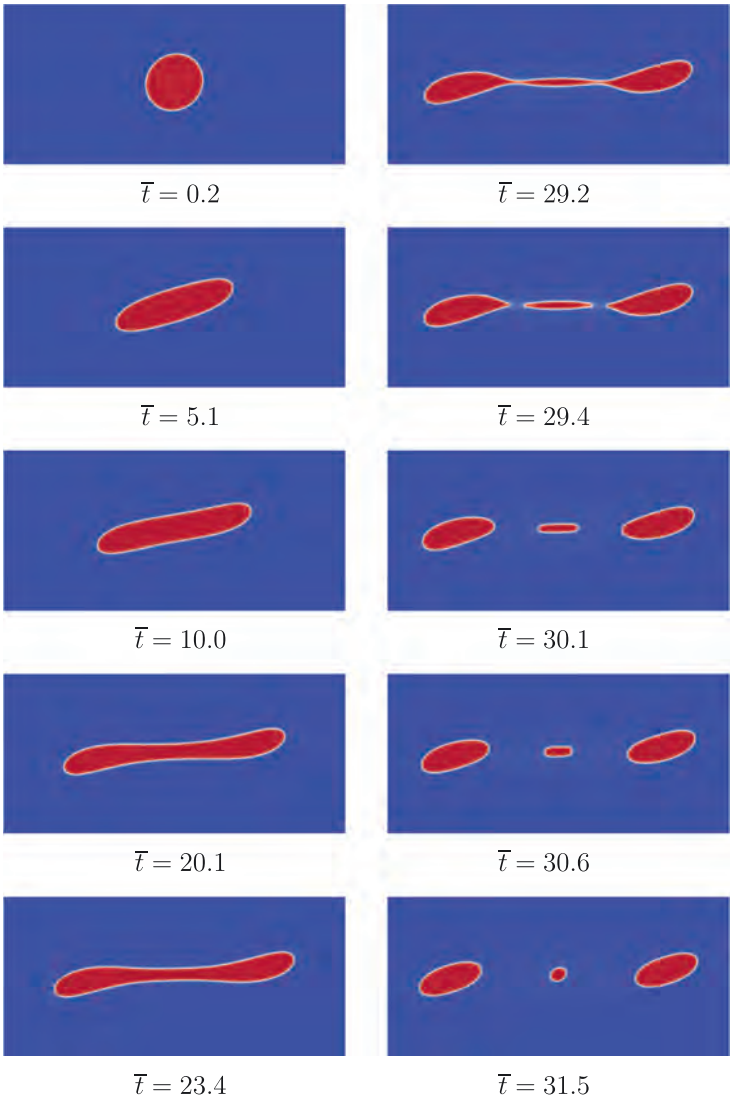

Fig. 9. Evolution of the drop shape at $\mathrm{Re} = 0.0625, \mathrm{Ca} = 0.42, \lambda = 1.0$ and initial drop radius $a = 30$ [lu] ($\overline{t} = t\dot{\gamma}$). The images only show a portion of the full domain.

Depending on the drop size, the duration of the simulations ranges from several minutes for the drops with lower resolution to 2–3 weeks for the drops with the highest resolution.

A simulation code for graphics processing units (GPUs) is used to facilitate convergence studies with large droplet radii (32–64 lattice units). The high memory bandwidth and parallel processing capabilities of GPUs allow fast LBM simulations due to the highly-local nature of free energy LBM calculations: only data from adjacent nodes is required to update each node in the domain. The simulations are performed on nine NVIDIA Tesla M2070 GPUs, with three GPUs installed on each of three computational nodes. Communication between the three GPUs on one computational node occurs over system buses, while communication between computational nodes occurs over an InfiniBand interconnect and was implemented with an MPI library. The domain is split evenly among the nine GPUs along planes parallel to the sheared wall. A rotational symmetry boundary condition through the middle of the domain ($y = H/2$ in Fig. 2) is used to further reduce the computational expense. With this boundary condition, the domain below $y = H/2$ is not simulated. Since the GPU code was initially developed to study a different problem, binary droplet collisions and coalescence (Shardt et al., 2013), the boundary conditions in the GPU code differ subtly from those in the CPU code. The shear velocity at $y = H$ is imposed using the method of Ladd (1994). A symmetry condition is used for the phase field ϕ at $y = H$. The other symmetry and periodic boundary conditions are the same as in the code for CPUs. Two simulations at the same conditions, with one running on GPUs and the other on CPUs, were compared. As described in Appendix B, the difference in the drop elongation L/a (see definition below) is 0.15%. The difference in boundary conditions is therefore small, and the GPU and CPU simulations may be used to study the same problem. Processing speeds for the simulations with droplet radii between 32 and 64 lattice units are 136–235 million lattice node updates per second (Mlups), compared to 2 Mlups on 8 CPU cores in the CPU-based simulation. The performance of both GPU- and CPU-based simulations is affected by other jobs running on the clusters, causing fluctuations in the processing speeds.

4.1. Choice of numerical parameters

A set of three physical dimensionless numbers (the Reynolds number Re, the capillary number Ca and the fluids' viscosity ratio λ, see definitions (1)) fully determines drop behavior under simple shear flow. The lattice Boltzmann free energy method refers to the class of diffuse interface methods that requires an explicit specification of the interface thickness ξ and related numerical parameters (κ, A, M, Γ). Two additional dimensionless numbers need to

be introduced to characterize these degrees of freedom (Van der Sman and van der Graaf, 2008): the interface Peclet number that relates the convection time scale to the interface diffusion time scale

$$Pe = \frac{\dot{\gamma} a \xi}{M A} \tag{17}$$

and the Cahn number which is the ratio between interface thickness and drop radius

$$Ch = \frac{\xi}{a} \tag{18}$$

Thus, the behavior of the same drop in simple shear flow in numerical space is determined by five dimensionless numbers, three of which are physical $(\mathrm{Re}, \mathrm{Ca}, \lambda)$ and two are numerical (Pe, Ch). It is necessary to investigate the choice of these numerical numbers to capture the drop behavior at given physical dimensionless numbers. The verification of the numerical technique involves an investigation of the influence of the Peclet and Cahn numbers on accuracy and stability. Subsequently the technique is validated by comparison with available literature data.

When the sheared drop evolves to a steady shape under Stokes flow conditions, two parameters are used to measure the deformation attained by the drop. The first parameter is the Taylor deformation parameter (Taylor, 1932, 1934) $D = (L - B)/(L + B)$, where L and B are the half-length and half-breadth of the drop (see Fig. 3), respectively. When the steady shape of the drop is not ellipsoidal any more (which is the case for shear with higher Re) then the ratio of maximum elongation to initial undeformed drop radius L/a is used to characterize the deformation. The second parameter is the orientation angle θ of the drop as defined in Fig. 3.

The influence of the proximity of walls was examined first. Three simulations of a drop with initial radius of $a = 20$ [lu] at $\mathrm{Re} = 1, \mathrm{Ca} = 0.27, \lambda = 1, Pe = 1$ and $Ch = 0.057$ were carried out in domains of $8a \times 4a \times 2a, 8a \times 8a \times 2a$ and $8a \times 12a \times 2a$. According to the VOF results presented by Renardy and Cristini (2001a) this capillary number (for given Re and λ) is right below the Ca_c which means that a steady shape of the drop is attained. The results of the present simulations together with the reference VOF results are presented in Table 1. The smallest distance between the plates $H = 4a$ results in higher deformation of the drop and significantly smaller inclination angle. The effect of H reduces when H is increased. The deviation between results obtained in the cases when $H = 8a$ and $16a$ is less than 3%. Simulation time increases with domain size. Further benchmark cases used domains of $8a \times 8a \times 2a$.

Three benchmark cases have been performed characterized by the following dimensionless numbers, respectively: $\mathrm{Re} = 1$ and $\mathrm{Ca} = 0.27, \mathrm{Re} = 0.0625$ and $\mathrm{Ca} = 0.1, \mathrm{Re} = 10$ and $\mathrm{Ca} = 0.15$. The viscosity ratio for all cases was $\lambda = 1$.

Consider the first case: $\mathrm{Ca} = 0.27, \mathrm{Re} = 1, \lambda = 1$. The relaxation times for both distribution functions are set to $\tau_f = \tau_g = 1$. The reference VOF results are presented in Table 1.

Mesh refinement was performed at different Peclet and Cahn numbers. The full set of dimensionless parameters $(\mathrm{Re}, \mathrm{Ca}, \lambda, Pe$ and $Ch)$ remained constant when the resolution was increased. The simulated Cahn numbers are $Ch = 0.1136$ and 0.2, the baseline drop radius is $a = 10$ [lu]. The mesh is refined by factors of β = 1.5, 2.0, 2.5 and 3.0 times. The resulting drop radii are 15, 20, 25, and 30 [lu]. Peclet numbers of 1, 5 and 10 are simulated.

The drop elongation and orientation angle for $Ch = 0.1136, 0.2$ and several Pe are presented in Fig. 4(a) and (b), respectively. For the reference points obtained by Renardy and Cristini (2001a), the initial drop radius spanned eight dimensionless units (grid spacing). When the grid is refined, the L/a tends to reach asymptotic values. At $Ch = 0.1136$ and $Pe = 10$ the deviation of the elongation from the reference data is 2% when $a = 30$ [lu]. The orientation angle is more sensitive and grid convergence is not clear. The θ values scatter within 20% from the reference data. The minimum deviation is 0.4% at $Ch = 0.2, Pe = 10$ and $a = 30$ [lu]. A smaller Peclet number results in smaller deformation and larger inclination angle of the drop. At $Pe = 1$ and $Ch = 0.2$ the simulations of drops with radius in the range 10–30 [lu] are unstable. When the drop radius exceeds 20 [lu] the simulations are unstable at $Pe = 1$ and 5. The reason for this instability is the high mobility value M. Mobility enters the governing system of equations via the mobility coefficient Γ (see Eq. (2c)) and has an impact on stability of the simulations. For the unstable cases Γ is larger than 15. On the other hand, drops with $a < 15$ [lu] break up at $Pe = 5$ and 10. High Pe means a low mobility M. In order to maintain local equilibrium, the mobility coefficient Γ (and thus mobility M) should be large enough to allow diffusion across the interface on a time scale faster than fluid motion (Kendon et al., 2001). Thus, when Γ is low then the convection dominates over diffusion (which tends to equilibrate the interface) and the droplets break. If a too large mobility value is set (see above), the simulations may become unstable.

To check if the influence of Pe and Ch is not a result of relatively low resolution ($a \leqslant 30$ [lu]), an additional study with highly resolved drops was carried out using the GPU code. A base-line drop radius of $a = 32$ [lu] is specified. The results are presented in

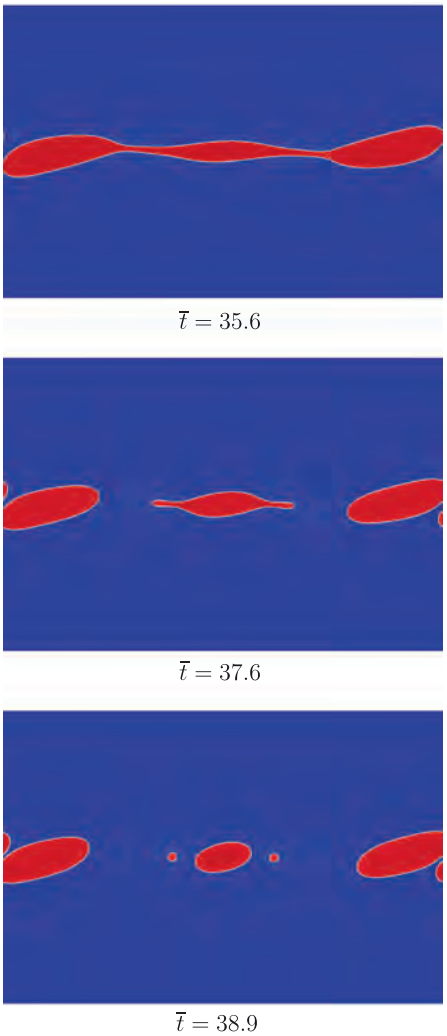

Fig. 10. Evolution of the drop shape at $\mathrm{Re} = 0.0625, \mathrm{Ca} = 0.42, \lambda = 1.0$ and initial drop radius $a = 64$ [lu] ($\bar{t} = t\dot{\gamma}$).

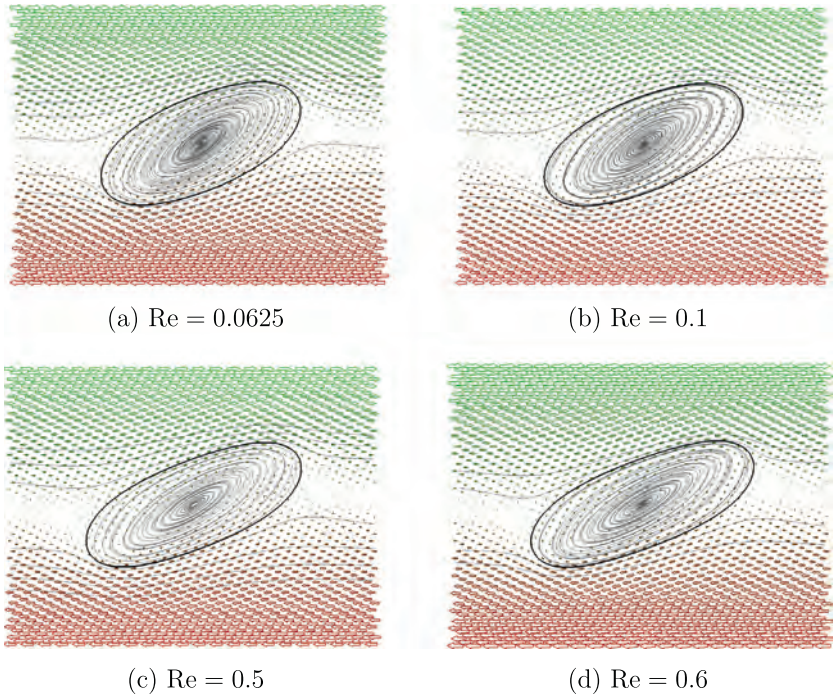

Fig. 11. Steady-state velocity field and drop shape for Ca = 0.3, $\lambda = 1$ and different Re numbers.

Appendix A (*Benchmark case 1*). The same trends in the effects of *Pe* and *Ch* on the results as with lower resolution are observed. Even with higher mesh resolution *Pe* and *Ch* should be chosen with care for every simulation. For instance, the case with $Pe = 1, a = 64$ [lu] (the Cahn number $Ch = 0.0625$) is unstable. While the case with $Pe = 1$ and higher drop resolution $a = 75$ [lu] (the Cahn number $Ch = 0.0267$) results in $L/a = 1.79$ and $\theta = 24.92^\circ$ that matches the reference data.

For flows with Re = 1, the shear rate is high enough to avoid long computations and a wide range of capillary numbers can be investigated due to κ, A and Γ values that allow stable computations. The Stokes flow regime needs to have very low shear (which implies small time steps and, thus, lengthy computations). It is also more challenging because of the narrow parameters ranges for stable simulations. To obtain capillary numbers in the range of 0.1–0.45, surface tension values in the range $\sigma = 10^{-4}$–10^{-3} [lu] are necessary. To fulfill this requirement, κ should also be small ($10^{-4} - 10^{-3}$ [lu]). To get stable simulations, special care should be taken for the choice of Γ and, consequently, the Peclet number. Simulations of drops in shear flow at near Stokes flow at Ca = 0.1 and $\lambda = 1$ were performed as the second benchmark case. The specified Reynolds number of Re = 0.0625 is the same as was taken by Li et al. (2000) in their simulations by the VOF method. The latter are used as reference data.

The results of the second benchmark case at Re = 0.0625, Ca = 0.1 and $\lambda = 1$ are presented in Appendix A (*Benchmark case 2*). The order of magnitude of the Peclet number for the Stokes flow simulations has changed compared to the one at Re = 1 considered before. *Pe* is less than unity now. The reason is a decrease of shear rates while the rest of the parameters have the same order of magnitude as before. The same influence of *Pe* on drop deformation is observed. The higher the Peclet number the higher the deformation and the smaller the inclination angle of the drop.

To check the ability of the method to handle higher Reynolds numbers, a third benchmark case was performed. The following physical parameters are specified: Re = 10, Ca = 0.15 and $\lambda = 1$.

Table 2
Deformation parameter for different Re numbers, Ca = 0.3, $\lambda = 1.0$

Re	0.0625	0.1	0.5	0.6
D (LBM)	0.396	0.399	0.454	0.469
D (VOF) (Li et al., 2000)	0.372	0.3968	0.45	0.4768

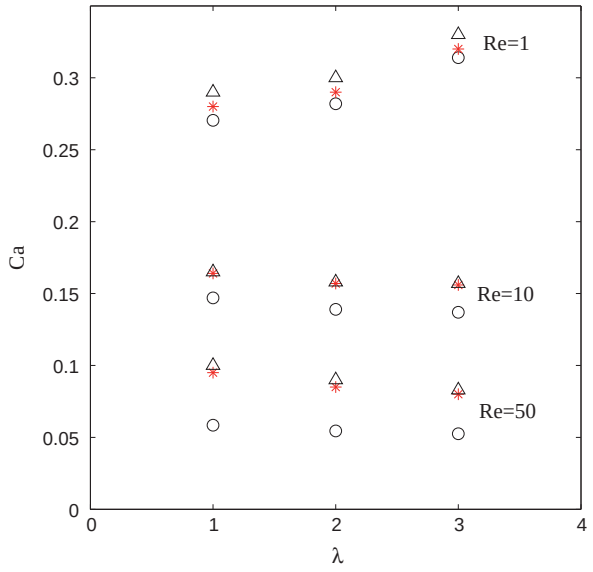

Fig. 12. Capillary number Ca as a function of viscosity ratio λ. Present simulations with free energy LBM: ✳ Ca for which drop attains steady shape; △ Ca for which drop breaks up; ○ critical capillary numbers Ca_c obtained by VOF method (Khismatullin et al., 2003).

The results and analysis are presented in Appendix A (*Benchmark case 3*). To sum up the most important findings, the influence of *Pe* and *Ch* on the result for a fixed drop radius of $a = 30$ lattice units is shown in Fig. 5. The data are organized in the following way: the

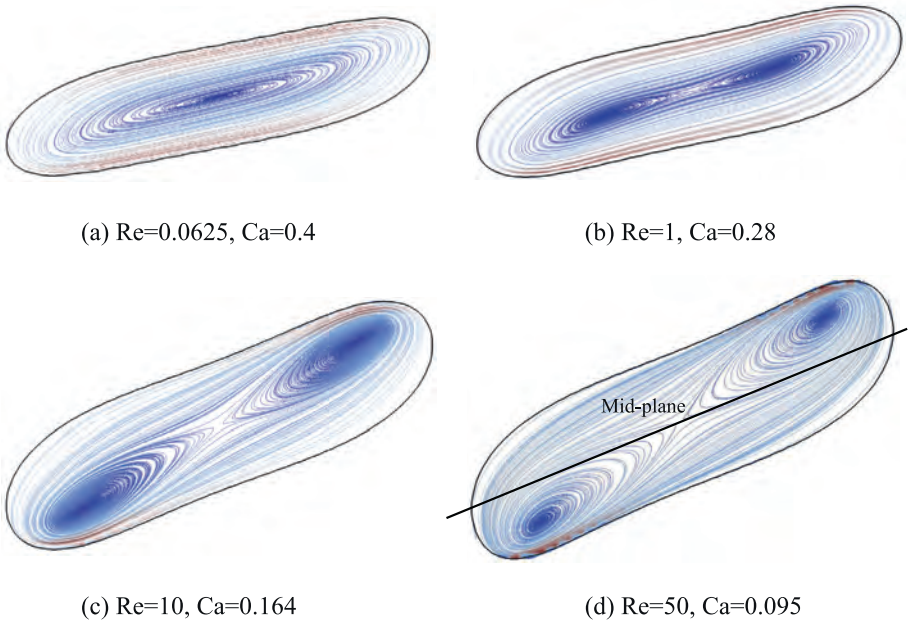

Fig. 13. Drop shape and velocity field inside the drop for different Reynolds numbers Re and near critical capillary number Ca for each Re ($\lambda = 1$); $Ch = 0.0568$; (a) $Pe = 0.41$; (b) $Pe = 1.45$; (c) $Pe = 1$; and (d) $Pe = 4.15$.

Peclet number increases from left to right, while the Cahn number increases from top to bottom. An increase in *Pe* results in increased drop deformation for every case: the drop becomes more elongated. The angle of inclination towards the flow direction decreases with the increase in *Pe*. The increase of interface thickness apparently limits drop deformation and the development of internal circulations; the drop shortens and aligns in a vertical direction. Re = 10 is not high enough to clearly see the loss of symmetry over the mid-plane of the drop. Nevertheless, it can be noticed for the case with $Pe = 4$ and $Ch = 0.0379$. The tips of the drop are slightly tilted in the vertical direction. If this deformation is accurately resolved then the maximum elongation of the drop refers to the line that connects these two point. The angle of inclination will be accordingly measured between this line and the horizontal axis. On the other hand, the elongation can be measured based on the mid-plane line. That will give a smaller value of elongation and a smaller angle of inclination. In the present simulations, maximum elongation was measured based on the tips of the drop. This contributes to the deviations from the reference data.

The aim of the benchmark studies is to establish guidelines on how to specify the numerical parameters related to the interface thickness (*Pe* and *Ch*) for a given set of physical dimensionless numbers (Re, Ca and λ). The following conclusions are drawn. For every simulation one has to make a choice for drop resolution (fix the drop radius a in lattice units). With a set, the interface thickness ξ has to be specified. In other words, the Cahn number should be chosen. For the present simulations, the drop resolution can be divided into two regions based on the drop radius: moderately resolved drops with $a \leqslant 30$ lattice units and highly resolved drops with radius $a > 30$ [lu]. The drop radius of 30 lattice units was chosen because starting from this radius the results are in the mesh independent region (see Figs. 4 and A.19). For the drops of moderate resolution a thinner interface is preferable. In the present study $\xi = 1.14$ [lu] (see Kendon et al. (2001)) was adopted. For the highly resolved drops a thicker interface of two lattice units needs to be used.

Thus, the choice of *Ch* is related to the resolution. Now the Peclet number should be chosen. This number contains the following parameters: $a, \xi, \dot{\gamma}, M$ and A. The first two (a and ξ) are already set.

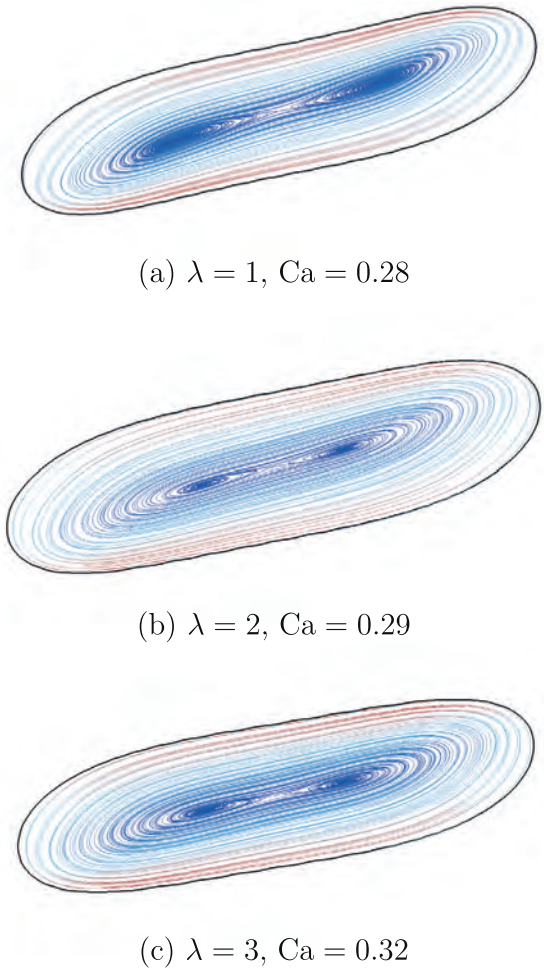

Fig. 14. Drop shape and internal circulations at Re = 1 and near critical capillary number for each λ; $Ch = 0.0568$; (a) $Pe = 1.45$; (b) $Pe = 1.5$; and (c) $Pe = 1.65$.

The shear rate $\dot{\gamma}$ is fixed by the Reynolds number. The parameter A is related to ξ and κ by Eq. (11). The interface thickness ξ is specified, while κ is fixed by the capillary number, which means A has been set as well. The only tunable parameter left is the mobility M that enters the governing equations as the mobility coefficient Γ (Eq. (8)). The diffusion over the interface should be faster than the fluid motion. According to Kendon et al. (2001) the mobility coefficient must be high to allow this. When a thicker interface is used, the residual diffusion contaminates more of the area around the drop. The effect of contamination is shown in Fig. 6. The areas inside and outside of the drop near the tips are more contaminated when higher Γ with thicker interface is used (Fig. 6(b)): one can see the lighter gray area. To clearly show the difference between these two cases the ϕ distribution along the horizontal lines is plotted on the graph in Fig. 6. The drop edges are sharper in case (a) compared to case (b). This effect decreases when a higher drop resolution is used (because the ratio of the interface thickness and the drop size is now smaller). For this reason the smaller interface thickness is utilized for the lower resolved drops, and a thicker interface for the higher resolution simulations.

Furthermore, the choice of the mobility coefficient (and consequently Pe) has influence on stability. In most of the cases the simulations are stable for Γ in the range 1–15. Smaller Γ results in more deformation of the drop which can lead to breakup when a steady shape is expected. On the other hand, too high mobility can cause instability. Based on the simulation results obtained here, the smaller the surface tension value (small κ) the higher Γ is needed.

Thus, the results of the benchmark cases show that the simulations are seemingly unpredictable and dependent on Peclet and Cahn numbers. Does it mean that to obtain a trustworthy physical result one has to perform several verification simulations and figure out Pe and Ch? To answer this question, different physical systems are further considered. In most of the simulations the Cahn number is fixed to $Ch = 0.0567$. The Peclet number varies from case to case while the mobility coefficient Γ is set equal to 8 or 10. A wide range of Reynolds and capillary numbers and viscosity ratios is examined to cover different physical phenomena. First, drop deformation and breakup in near-Stokes flow are considered at different capillary numbers. Then inertial effects are investigated at higher Reynolds numbers. Finally, the combined influence of inertia and viscosity ratio is investigated. Most of the results are compared to available literature data. Using these simulations, it is shown that even simulations at moderate resolution can be used to study drop deformation in shear.

4.2. Stokes flow simulations

To validate the numerical code with existing literature data, near-Stokes flow ($\mathrm{Re} = 0.0625$) simulations of a single drop were performed for capillary numbers of Ca = 0.2, 0.3 and 0.4. The initial drop radius is 20 [lu] in a simulation domain of $8a \times 8a \times 2a$. The

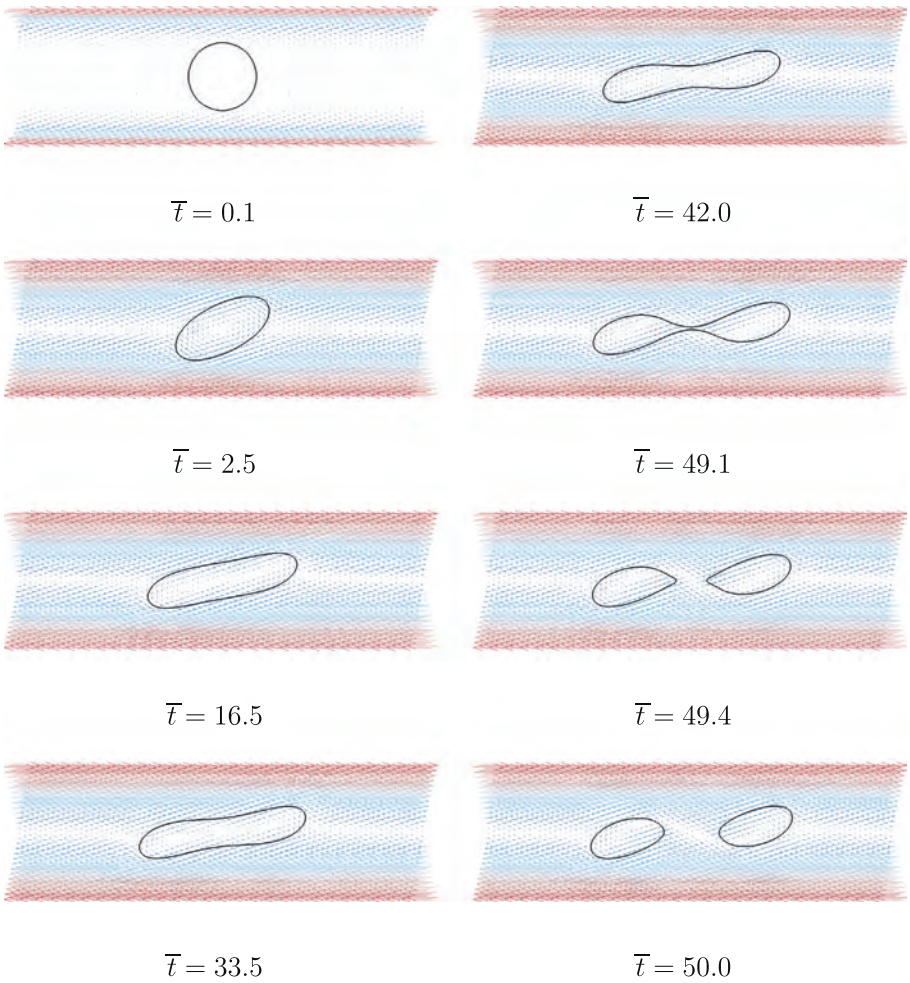

Fig. 15. Drop shape and velocity field change in time for $\mathrm{Re} = 1, \mathrm{Ca} = 0.3, \lambda = 2$ ($\bar{t} = t\dot{\gamma}$). Initial drop radius $a = 20$ [lu]; the Cahn number $Ch = 0.0568$, the Peclet number $Pe = 1.55$.

Cahn number is fixed to $Ch = 0.0567$ and the Peclet numbers are $Pe = 0.2$, 0.3 and 0.41 for each case, respectively.

The drop deformation D and orientation angle θ in steady state as a function of the capillary number Ca along with experimental and numerical results from the literature are depicted in Fig. 7(a) and (b), respectively. Our results agree well with the reference data. However, as discussed in the previous section, the results can be adjusted by variation of the Peclet number (or the diffusion coefficient Γ). Since the reference values of deformation and orientation angles are scattered, it is demonstrated that choosing Γ from the stable interval (1–15) gives the results that match reference data. Fig. 8 shows cross sections of the drop steady shapes and velocity fields in the $z = 0$ plane (see Fig. 2) for Ca = 0.1, 0.2, 0.3 and 0.4. The larger the capillary number, the stronger the drop deformation and the smaller the inclination angle.

To check the ability of the method to capture the breakup event, the following situation was simulated: $\mathrm{Re} = 0.0625, \mathrm{Ca} = 0.42$ and $\lambda = 1$. Based on experiments and available numerical results the critical capillary number for liquids with equal viscosities in the Stokes regime (Li et al., 2000) is $\mathrm{Ca}_c = 0.41$. Thus, for $\mathrm{Ca} = 0.42$ breakup is expected. According to a reference VOF result (Li et al., 2000) (see their Fig. 11) five fragments are formed: two daughter drops, one satellite droplet and two sub-satellites. To resolve these fragments a resolution higher than $a = 20$ [lu] is required. The initial drop radius is set to 30 [lu] in a simulation domain of size $12a \times 8a \times 2a$ (the same size as in VOF reference data). The Cahn number of $Ch = 0.0379$ and the Peclet number of $Pe = 0.43$ are specified. The results are presented in Fig. 9 where the drop shape evolution in time is depicted. The simulated drop breaks up forming two daughter drops and one satellite droplet between them. The mesh in this simulation is not sufficiently fine to resolve sub-satellite drops. Further refinement (to $a = 64$ [lu] with $Pe = 0.43$ and $Ch = 0.0177$) shows the formation of sub-satellites after breakup as also reported by Li et al. (2000). The final stages of the drop shape evolution over time are presented in Fig. 10. The drop deforms sufficiently to reach and wrap around the ends of the periodic domain, whose size was chosen to be the same as in (Li et al., 2000). Though the domain is too small to represent the behavior of a single drop in an unbounded domain, the simulation demonstrates the ability of the method to resolve sub-satellite drops during the breakup of the thread.

4.3. Influence of inertia

In order to capture drop deformation and breakup at higher Reynolds numbers, three simulations were performed at a capillary number of $\mathrm{Ca} = 0.3$ and Reynolds numbers $\mathrm{Re} = 0.1, 0.5$ and 0.6 (the Reynolds numbers are taken the same as in the reference data by Li et al. (2000)). The initial drop radius is $a = 20$ [lu] in a simulation domain of $8a \times 8a \times 2a$. The Cahn number is $Ch = 0.0568$ and the Peclet numbers are $Pe = 0.31, 0.39$ and 0.39 for each Re, respectively. The Reynolds number is increased by increasing the velocity of the wall while keeping the viscosity of both liquids equal to $\nu_d = \nu_c = 1/6$ (relaxation time $\tau_f = 1.0$).

For a fixed capillary number, an increase in the Reynolds number leads to higher drop deformation, the drop changes its shape

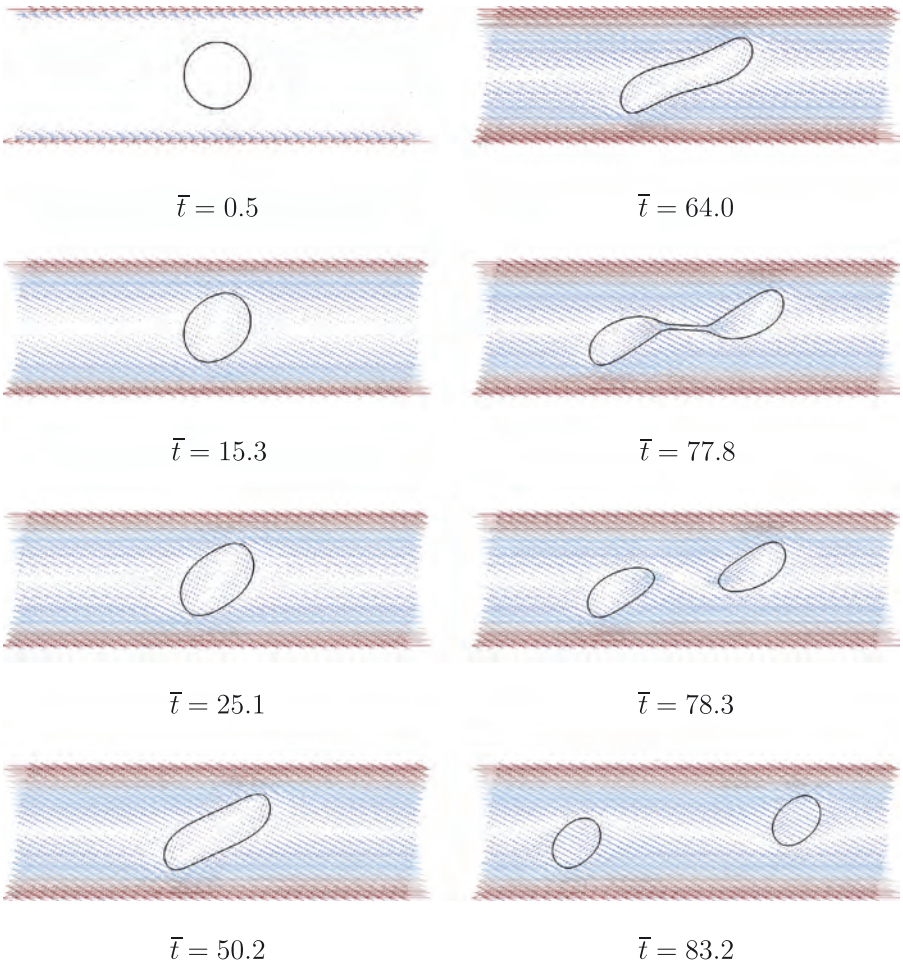

Fig. 16. Drop shape and velocity field change in time for $\mathrm{Re} = 50, \mathrm{Ca} = 0.09, \lambda = 2$ ($\bar{t} = t\dot{\gamma}$). Initial drop radius $a = 20$ [lu]; the Cahn number $Ch = 0.0568$, the Peclet number $Pe = 3.93$.

from ellipsoidal to elongated. The drop shape at steady state together with velocity fields is illustrated in Fig. 11 for $\mathrm{Re} = 0.0625, 0.1, 0.5$ and 0.6. The results are in qualitative agreement with those presented by Li et al. (2000) (see their Fig. A.18). The deformation parameter D, simulated using LBM, is listed in Table 2 for different Re together with the results obtained using the VOF method (Li et al., 2000). The deviation between the D values is less than 1%.

4.4. Joint influence of viscosity ratio and inertia

To demonstrate that different liquid viscosities can be handled, a set of simulations has been performed and the results have been compared to the VOF results reported by Khismatullin et al. (2003).

The initial drop radius of $a = 20$ [lu] (at the Cahn number $Ch = 0.0567$) in a simulation domain of $12a \times 4a \times 2a$ is considered. The Peclet number varies in the range from 1 to 5. The relaxation time of the continuous phase is $\tau_f = 0.6$, and the relaxation time for the liquid in the droplet is adjusted based on the viscosity ratio λ.

The Reynolds numbers were Re = 1, 10 and 50. These are much higher Reynolds numbers than discussed so far. Khismatullin et al. (2003) reported critical capillary numbers as a function of viscosity ratio for these Re values. Since the critical capillary number was not known a priori, two capillary values were searched for every Re number: one for which the droplet attains steady state and the second one for which the drop breaks up and forms daughter droplets. In Fig. 12, Ca is plotted as a function of λ for the three Re numbers. The trends in Ca_c as a function of λ and Re found in the present study mimic the ones obtained using the VOF method (Khismatullin et al., 2003). However, with the increase of Re, the deviation in Ca_c values increases compared to the reference results. This can be attributed to the limited drop resolution. Grid refinement improves the results. For instance, when $\mathrm{Re} = 50, \lambda = 1$ the drop with initial radius $a = 64$ [lu] ($Ch = 0.03125$) attains a steady shape at $\mathrm{Ca} = 0.07$ and breaks at $\mathrm{Ca} = 0.08$. This result is in a better agreement with reference data.

To highlight the influence of inertia, the shapes of the drops for different Re together with internal circulations are shown in Fig. 13. Only the results for $\lambda = 1$ are presented here, but the conclusions are similar for $\lambda = 2$ and $\lambda = 3$. As one can see, with the increase of Re the steady shape of the drop is more towards the vertical direction. In Stokes flow, the drop is more symmetrical over the mid-plane with one vortex inside the drop. Inertia makes significant changes to the drop shape and velocity field: with the increase of Re the symmetry across the mid-plane vanishes and two vortices appear inside the drop (Fig. 13(d)). All these observations are in qualitative agreement with those reported by Renardy and Cristini (2001a).

The influence of the viscosity ratio can be analyzed using Fig. 14 where the shapes of the drop for Re = 1 and λ = 1, 2 and 3 with internal circulations at the near critical capillary number are depicted. The increase of the viscosity ratio means the drop becomes more viscous compared to the matrix liquid. Higher viscosity of the drop weakens circulation inside the drop: the vortex inside the drop in Fig. 14(a) is more developed compared to that shown in Fig. 14(c). The less viscous drop is more deformable: the symmetry over the mid-plane is lost for the drop with $\lambda = 1$ while the drop with $\lambda = 3$ is almost symmetric.

An increase of inertia also changes the breakup mechanism. To study the influence of the Reynolds number on breakup, simulations were performed for a system with viscosity ratio $\lambda = 2$, initial drop radius $a = 20$ [lu] for $\mathrm{Re} = 1$ and 50 and above the critical capillary numbers for each Re. The evolution of drop shape and velocity field when $\mathrm{Re} = 1$ is shown in Fig. 15. The drop stretches in the flow direction. Only one vortex is formed inside the drop

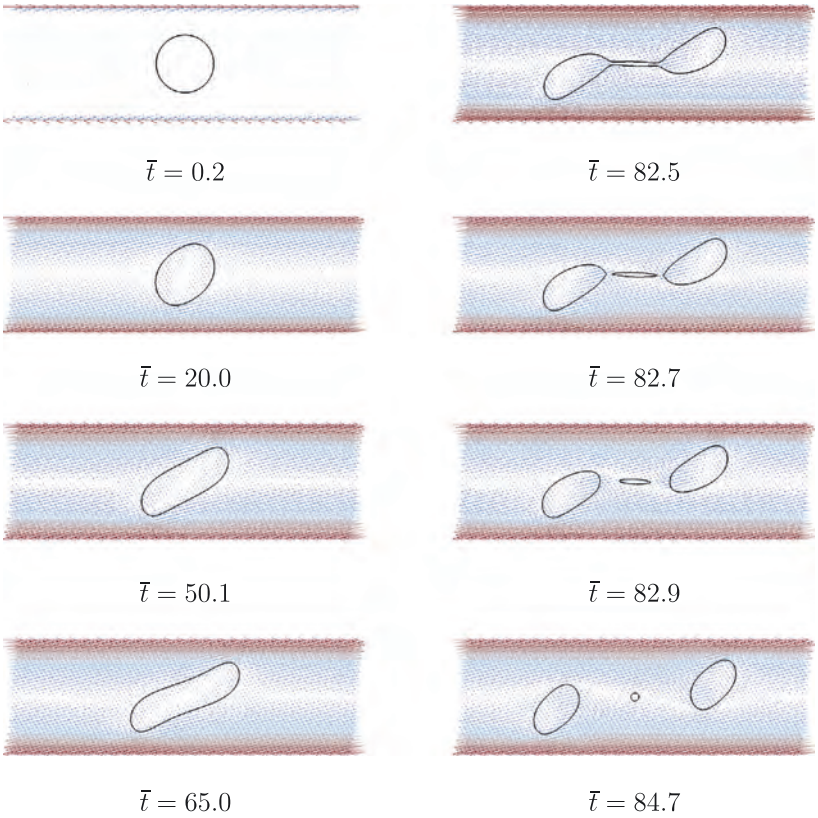

Fig. 17. Drop shape and velocity field change in time for $\mathrm{Re} = 50, \mathrm{Ca} = 0.085, \lambda = 2$ ($\bar{t} = t\dot{\gamma}$). Initial drop radius $a = 30$ [lu]; the Cahn number $Ch = 0.0379$, the Peclet number $Pe = 3.71$.

up to $\bar{t} = 2.5$. When the neck in the middle of the drops begins to form, two symmetric vortices appear. The neck gradually thins and the drop breaks up forming two daughter droplets.

If inertia is increased up to $\mathrm{Re} = 50$, significant changes in drop breakup take place (see Fig. 16). The tips of the drop are caught by streamlines with higher velocity that elongate the drop in the vertical direction. Two vortices are formed in the drop immediately after the start of the shear.

In addition, the influence of resolution was checked for $\mathrm{Re} = 50$. The resolution is increased such that $a = 30$ [lu]. The results are presented in Fig. 17. This time a satellite drop forms after breakup. Moreover, the critical capillary number decreased with the increase of resolution which means the results are in better agreement with reference data if simulated with higher resolution (see Fig. 12).

As one can see in Fig. 12, with the increase of inertia in the system even viscous drops are broken. For Stokes flow conditions, the critical capillary number significantly increases when λ approaches the value of 3. High Re numbers decrease the absolute value of critical capillary numbers and allow viscous drops to break.

5. Conclusions

Numerical simulations of a single liquid drops suspended in another liquid and subjected to simple shear flow have been presented. The free energy lattice Boltzmann method was used to perform three-dimensional simulations of the binary systems in order to determine the drop deformation and breakup conditions. During this study the numerical tool has been implemented, verified and validated with available reference data.

The full physical description of the problem requires three physical dimensionless numbers (the Reynolds number, the capillary number and the viscosity ratio). However, the description of the same problem in numerical space requires two additional dimensionless numbers. The adopted diffuse interface method involves the finite thickness of the interface between the two liquids and related free energy model parameters. These numerical degrees of freedom are characterized by two dimensionless numbers: the Peclet and Cahn numbers. The influence of these two numbers on accuracy and stability was investigated. A guideline on how to choose *Pe* and *Ch* in order to reveal physically realistic behavior of the drop at given Re, Ca and λ is presented below.

Three benchmark cases were performed to analyze the impact of *Pe* and *Ch*. A range of physical conditions was considered: starting from near Stokes flow and up to Reynolds of 10. The accuracy and stability are affected by the choice of *Pe* and *Ch*. A smaller Peclet number for a given Cahn number results in less deformation and smaller inclination angle of the drop. These effects hold for moderately and highly resolved drops. Correct physical behavior is captured in most of the cases.

For each benchmark case, mesh refinement studies were carried out for different sets of *Pe* and *Ch*. Two mesh refinement principles were considered. The first principle assumes keeping all five dimensionless numbers constant when the mesh is refined, while in the second mesh refinement principle four dimensionless numbers $(\mathrm{Re}, \mathrm{Ca}, \lambda, Pe)$ and the interface thickness remain the same. This principle follows the sharp-interface limit of Yue et al. (2010) where it is suggested to maintain the mobility value M while decreasing the Cahn number *Ch*. Different choices of the relationship between M and *Ch* might be optimal (see (Jacqmin, 2000; Magaletti et al., 2013)).

Both mesh refinement principles work: the key parameters (drop deformation and orientation angle) tend to reach asymptotic values. The results tend to mesh independency when the initial drop radius $a > 30$ lattice units. This drop size separates two regions of resolution: a region of moderate resolution when $a \leqslant 30$ [lu] and high resolution with $a > 30$ [lu]. However, for a given set of physical parameters $(\mathrm{Re}, \mathrm{Ca}, \lambda)$ and different numerical parameters (Pe, Ch), the asymptotic values may differ from each other: at one Peclet number the drop may attain a steady shape, while at another Peclet number the drop may eventually break at high resolution, or the simulation might be unstable at low resolution.

The accuracy of the results is mostly determined by the mesh resolution and can only be *adjusted* by varying *Ch* and *Pe*. Drops of moderate resolution require a thinner interface. The suggested value is 1.14 [lu] (in line with the results of Kendon et al. (2001)). For highly resolved drops a thicker interface is preferable (at least two lattice units). Thus, the interface thickness is set based on the researcher's preferences on mesh resolution. Now the Cahn number is known, the Peclet number needs to be set. It was shown that a *Pe* specification actually is the specification of the mobility M because the rest of the parameters involved in *Pe* are already determined by the physical dimensionless numbers and by *Ch*. The mobility value is determined by the mobility coefficient Γ. The present simulations and the observations of Kendon et al. (2001) have shown that to allow diffusion over the interface to occur faster than fluid motion, the mobility coefficient should be high enough. Based on the present results, the simulations are stable when the mobility coefficient is in the range 1–15. The thicker the interface the higher Γ values (i.e. smaller *Pe*) are required. If *Pe* is high then convection over the interface dominates diffusion and the interface breaks in cases where a steady state with one drop should be attained. On the other hand, too high Γ (usually $\gg 20$) might cause instability. If there is reference data then these can be used to find *Pe*. And then this *Pe* value can be used in further simulations. If the reference data is not available, it is suggested to select the mobility coefficient value from the stability range 1–15, then the deviation of numerical results will be within 20% for near-Stokes flow and less for Reynolds numbers of the order of one.

To demonstrate that even moderately resolved drops can be used to investigate the physics of drop deformation and breakup, further simulations were carried out. The drops of $a = 20$ and $a = 30$ [lu] were chosen with an interface thickness of 1.14 [lu]. These drops were exposed to a wide range of physical conditions ($\mathrm{Re} = 0.0625 - 50$). The mobility coefficient was equal to 10 in most of the cases.

The results of Stokes flow simulations for deformation and breakup agree well with the results of other numerical techniques such as VOF, boundary integral method and experiments. The deviation of deformation and orientation angle is within 20% for the capillary number range 0.1–0.4. Moderate drop resolution is not enough to capture sub-satellite drops after breakup at $\mathrm{Ca} = 0.42$. Highly resolved drops should be used. For relatively low Reynolds numbers ($\mathrm{Re} = 0.1, 0.5, 0.6$) and capillary numbers less than critical, the obtained drop deformation is in excellent agreement with VOF results presented by Li et al. (2000): the deviation of the drop deformation value is less than 1%. The ability of the code to handle different liquid viscosities at higher Re numbers was also tested. Even though the trend of the curves of capillary number as a function of viscosity ratio for different Reynolds numbers was captured, the deviation from VOF results (Khismatullin et al., 2003) increased for higher Re. It was demonstrated that a way to improve agreement is to increase the resolution of the LBM simulations.

The impact of the Peclet and Cahn numbers does not outweigh the valuable advantage of the utilized diffuse interface method over the interface tracking techniques: the feasibility to perform simulations of a system involving a high fraction of dispersed phase, i.e. large numbers of drops. The verified and validated numerical tool will be used for industrial applications. For example, for a given binary system of two liquids under applied shear

it is possible to determine the resulting drop size distribution (DSD). Or if the final product should have a certain DSD then the proper shearing conditions can be found. The advantage of numerical experiments is the possibility to visualize the entire flow. Moreover, one can modify and apply the operating conditions that are challenging to implement in a real experimental set-up. As for further steps, the developed tool will be extended for the dispersion formation simulations under turbulent flow conditions (Komrakova et al., in press).

Acknowledgements

This research has been enabled by the use of computing resources provided by WestGrid and Compute/Calcul Canada. O.S. is grateful for the support of an Alexander Graham Bell Canada Graduate Scholarship from NSERC. A.E.K. would like to thank Schlumberger for financial support of the research.

Appendix A. Benchmark cases

Benchmark case 1. Simulation parameters are $\mathrm{Re}=1, \mathrm{Ca}=0.27, \lambda=1$. To verify that at higher mesh resolution the same influence of *Pe* and *Ch* holds, mesh refinement cases were considered with the base-line drop radius of $a=32$ [lu]. The refinement factors of 1.5 and 2.0 gave drop radii of 48 and 64 [lu]. The Cahn numbers of $Ch=0.0355$ and 0.0625 at Peclet numbers of 1, 3 and 10 were examined.

The drop elongation and orientation angle are presented in Fig. A.18(a) and (b), respectively. When $Ch=0.0625$ and $Pe=1$ the simulations are unstable for $a=48$ [lu] ($\Gamma=34.56$ for this case). Breakup of the droplet takes place in the following cases: $Pe=1, Ch=0.0355$ and $a=32$ [lu]; $Pe=3, Ch=0.0355$ and $a\leqslant 48$ [lu]; $Pe=10, Ch=0.0625$ and $a\leqslant 48$ [lu]. Thus, the same trends with *Pe* on the results as at lower mesh resolution are observed: higher Peclet numbers lead to more deformation and smaller inclination angle of the drop.

Benchmark case 2. Simulation parameters are $\mathrm{Re}=0.0625, \mathrm{Ca}=0.1, \lambda=1$. The relaxation times for both distribution functions were set to $\tau_f=\tau_g=1$.

In what follows two mesh refinement principles are considered. In the first mesh refinement principle all dimensionless parameters are kept constant (physical Re, Ca and λ and numerical *Pe* and *Ch*). The second mesh refinement principle assumes keeping Re, Ca, λ, *Pe* and ξ the same when the mesh is refined. The thickness of the interface is a numerical artifact and the reasoning is that *Ch* should approach zero when the grid is refined thereby approaching the real (physical) situation. This mesh refinement principle can be considered as approaching the sharp-interface limit (Yue et al., 2010). Both principles are tested further. A base-line drop radius of 10 [lu] was chosen. The refinement factors β were 1.5, 2.0, 2.5 and 3.0. The first principle was tested at $Pe=0.1$ and $Ch=0.1136$. The second one was performed with fixed interface thickness of $\xi=1.14$ [lu] and different *Pe* numbers of 0.07, 0.1 and 0.2.

The results of drop deformation and orientation angle for the Stokes flow simulations are presented in Fig. A.19(a) and (b), respectively. Convergence for increased resolution towards an asymptotic value is observed in each case. This means that both mesh refinement principles work: upon refinement the solution tends to become mesh independent. However, at $Pe=0.1, Ch=0.1136$ and $a=30$ [lu] the simulations are unstable.

When $a\geqslant 20$ [lu] and constant interface thickness $\xi=1.14$ [lu] the deformation results *D* agree well between different *Pe*. In addition, the deformation *D* is in a good agreement with the reference VOF result (the deviation is less than 1% for the finest drops). However, the deviation of the orientation angle θ from the reference data is around 20%.

Benchmark case 3. Physical simulation parameters are $\mathrm{Re}=10, \mathrm{Ca}=0.15, \lambda=1$. This capillary number is right below the critical value for the given Re as discussed by Renardy and Cristini (2001a). The reference VOF results (Renardy and Cristini, 2001a) have $L/a=1.9$ and $\theta=23^\circ$. To obtain the required Re, the viscosity of the liquids was lowered by setting the relaxation time to $\tau_f=0.56$. A mesh refinement procedure was performed with a base-line drop radius of $a=20$ [lu]. The refinement factors were $\beta=1.5$ and 2.0 (drop radii of 30 and 40 lattice units). The Cahn numbers were 0.0568 and 0.1. Also the second mesh refinement principle was tested with two constant interface thickness $\xi=1.14$ and 2.0 lattice units.

The simulation results are organized in Fig. A.20 and A.21 where the L/a ratio and the orientation angle θ are plotted versus drop radius *a*, respectively. In Figs. A.20(a) and A.21(a) the results of the

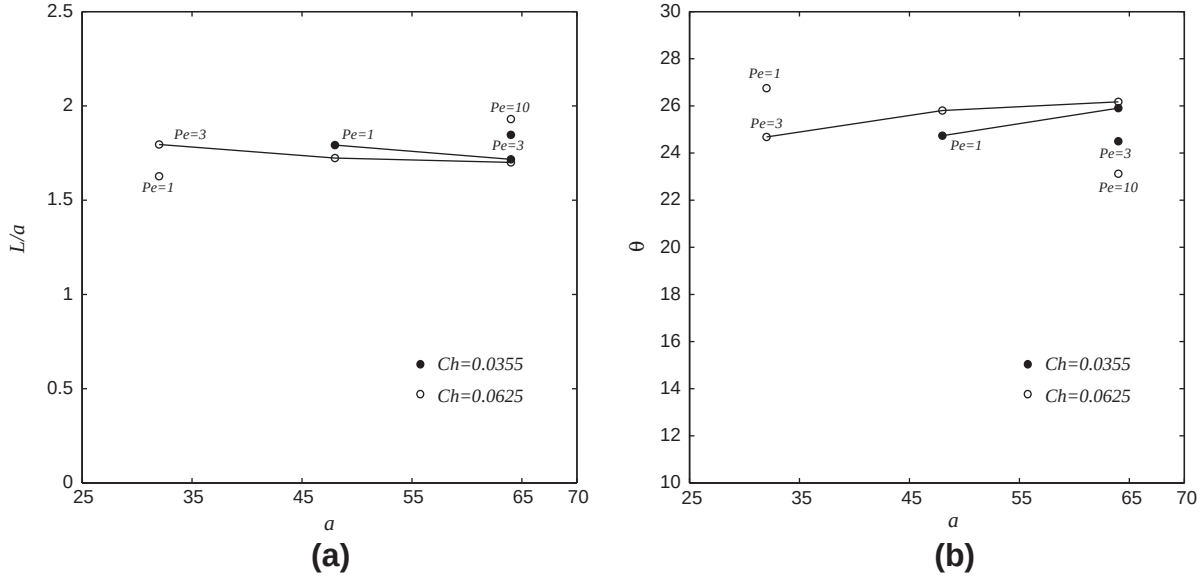

Fig. A.18. Drop deformation results at $\mathrm{Re}=1, \mathrm{Ca}=0.27, \lambda=1$ and different *Pe* and *Ch* numbers. The L/a ratio (a) and the orientation angle θ (b) as a function of drop radius (Benchmark 1).

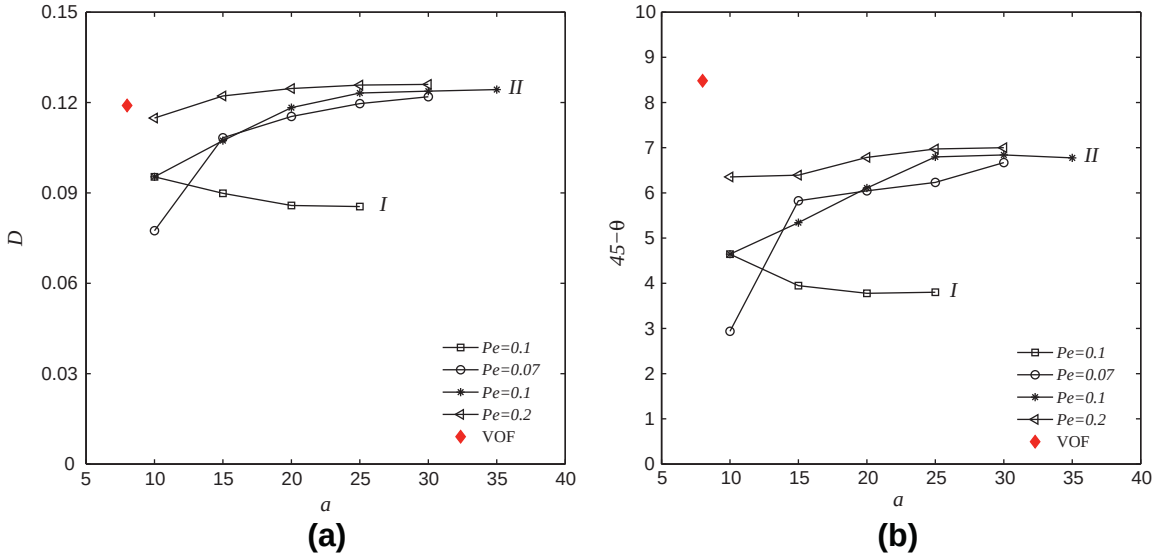

Fig. A.19. Drop deformation D (a) and orientation angle of a drop θ (b) for different drop radius a at $\mathrm{Re} = 0.0625, \mathrm{Ca} = 0.1$ and $\lambda = 1$; I first principle of mesh refinement at $Ch = 0.1136 = const$; II second principle of mesh refinement with $\xi = 1.14 = const$. Reference VOF computations of Li et al., 2000 are $D = 0.119$ and $(45 - \theta) = 8.48^\circ$ (Benchmark 2).

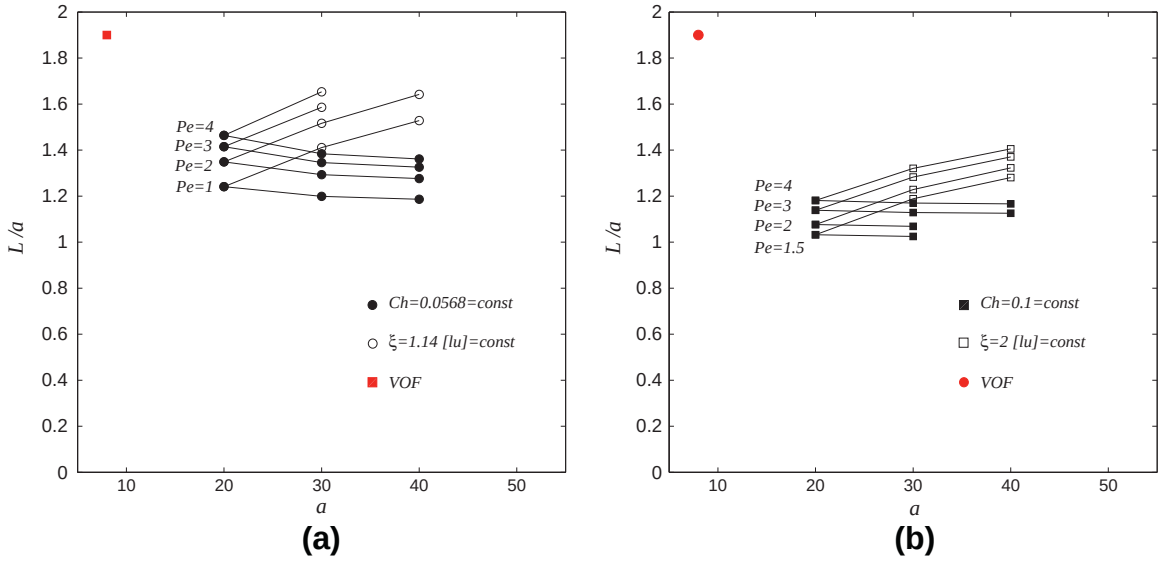

Fig. A.20. Elongation of a drop L related to initial drop radius a for different drop radii. $\mathrm{Re} = 10, \mathrm{Ca} = 0.15, \lambda = 1$. Cases denoted by •, ■ refer to the first principle of mesh refinement; cases denoted by ○, □ refer to the second principle of mesh refinement (Benchmark 3).

first principle at $Ch = 0.0568$ and the second one with fixed $\xi = 1.14$ [lu] at different Pe numbers are shown. The plot in Figs. A.20(b) and A.21(b) shows similar results but for constant $Ch = 0.1$ and the fixed interface thickness in 2 [lu]. A significant difference form the reference data is observed for both deformation parameters. However, the reference results of Renardy and Cristini (2001a) show unexpected non-monotonic trends. Renardy and Cristini (2001a) present L/a and θ as functions of the Reynolds number ranging from 0.0625 to 100. The results at $\mathrm{Re} = 10$ and $\mathrm{Ca} = 0.15$ deviate from the general trend: by interpolation of nearby results a smaller value of L/a and a higher θ would be expected. For example, Renardy and Cristini (2001a) show $L/a = 1.8$ and $\theta = 25^\circ$ at $\mathrm{Re} = 1$ and $\mathrm{Ca} = 0.27$. At $\mathrm{Re} = 60$ and $\mathrm{Ca} = 0.053$ the result is $L/a = 1.52$ and $\theta = 53^\circ$. In both cases the capillary number is sub-critical. Thus, for the case at $\mathrm{Re} = 10$ and $\mathrm{Ca} = 0.15$ an elongation between 1.52 and 1.8 is expected since the drop shortens as Re increases. Similarly, an orientation angle between 25° and 53° is expected because the drops tend to align more vertically for higher Re. In addition, the deviation between the present and reference data can be minimized if the Peclet number is increased.

The results based on the first mesh refinement principle (constant Ch) converge marginally better than the results based on the second one (constant ξ). The simulations of the drops with $a = 40$ [lu] and fixed $\xi = 1.14$ [lu] at $Pe = 3$ and 4 resulted in breakup. The reason is a low mobility coefficient Γ. When $a = 40$ [lu] and $Ch = 0.1 = const$ at $Pe = 1.5$ and 2 the simulations are unstable because of a too high Γ value ($\Gamma = 107$ and 80, respectively). Drops are more deformed if they have a thinner interface. In addition an increase in Pe leads to an increase of deformation. The droplets incline more when Pe is smaller.

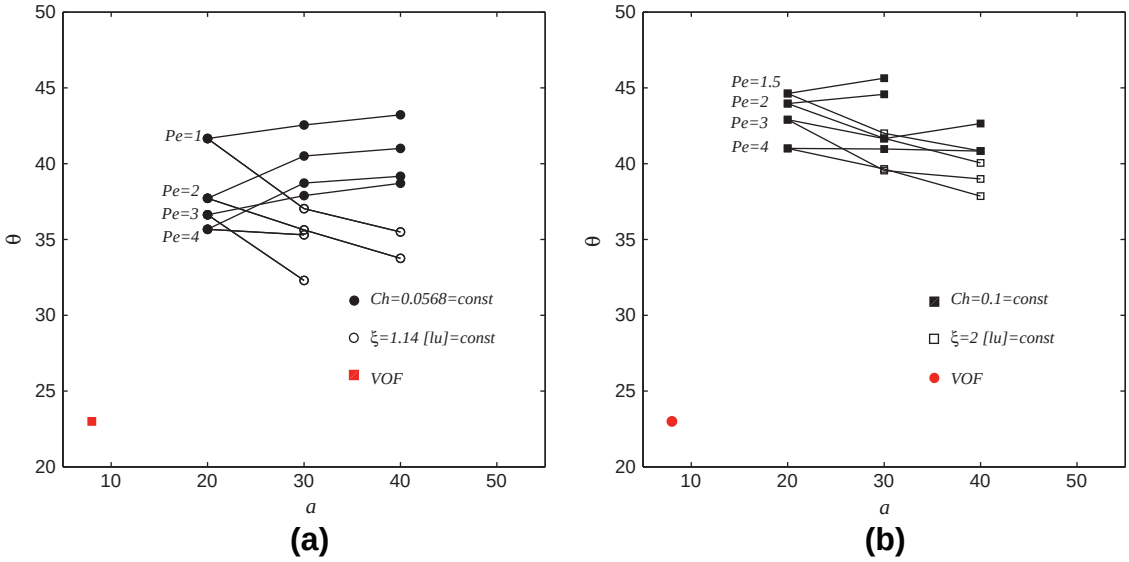

Fig. A.21. Orientation angle of a drop θ for different drop radii. Re $= 10$, Ca $= 0.15$, $\lambda = 1$. Cases denoted by $\bullet, \blacksquare$ refer to the first principle of mesh refinement; cases denoted by $\circ, \square$ refer to the second principle of mesh refinement.

(a) $a = 20$ [lu], $\xi = 1.14$ [lu], $Ch = 0.0568$

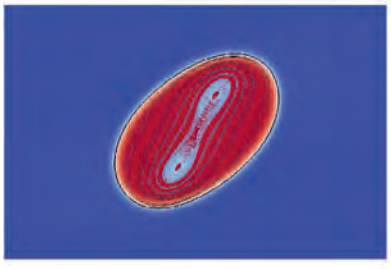

(b) $a = 30$ [lu], $\xi = 1.7$ [lu], $Ch = 0.0568$

(d) $a = 30$ [lu], $\xi = 1.14$ [lu], $Ch = 0.0379$

(c) $a = 40$ [lu], $\xi = 2.28$ [lu], $Ch = 0.0568$

(e) $a = 40$ [lu], $\xi = 1.14$ [lu], $Ch = 0.0284$

Fig. A.22. Drop shape (ϕ field) and streamlines at steady-state at Re $= 10$, Ca $= 0.15$, $\lambda = 1$, $Pe = 1$ and different Ch numbers: (a)–(c) the first principle of mesh refinement; (a), (d), (e) the second principle of mesh refinement (Benchmark 3).

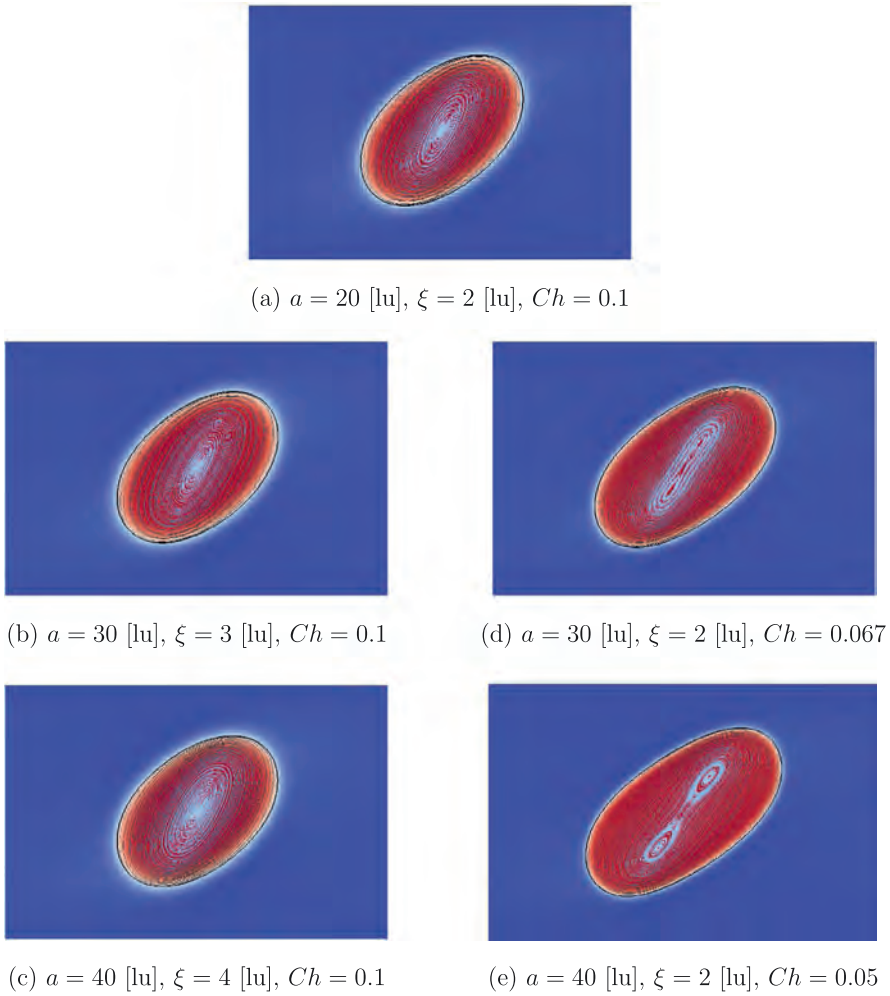

(a) $a = 20$ [lu], $\xi = 2$ [lu], $Ch = 0.1$

(b) $a = 30$ [lu], $\xi = 3$ [lu], $Ch = 0.1$

(d) $a = 30$ [lu], $\xi = 2$ [lu], $Ch = 0.067$

(c) $a = 40$ [lu], $\xi = 4$ [lu], $Ch = 0.1$

(e) $a = 40$ [lu], $\xi = 2$ [lu], $Ch = 0.05$

Fig. A.23. Drop shape (ϕ field) and streamlines at steady-state at Re $= 10$, Ca $= 0.15$, $\lambda = 1$, $Pe = 4$ and different Ch numbers: (a)–(c) the first principle of mesh refinement; (a), (d), (e) the second principle of mesh refinement (Benchmark 3).

In the Stokes flow limit, only one vortex forms inside the drop (see Fig. 8). The drop inclines towards the flow direction and has an ellipsoidal shape. With increasing Reynolds number, three major events take place (Renardy and Cristini, 2001a). First, the drop becomes more aligned with the vertical axis and shortens in the horizontal direction. Second, two vortices appear in the drop. And the third change is that the symmetry over the mid-plane at steady state is lost (see Fig. 13). These effects can also be observed in Fig. 5(c) presented by Renardy and Cristini (2001a). To validate the present numerical technique, the velocity field inside the drop was compared to the reference data.

In Fig. A.22 the drop shapes together with streamlines inside the drop are plotted for the cases with $Pe = 1$ for two types of mesh refinement: (a)–(c) fixed $Ch = 0.0568$ (the first principle); (a), (d), (e) fixed interface thickness $\xi = 1.14$ [lu]. $Pe = 1$ has been chosen because the drop does not break in the entire range of drop radii. The black curves in Fig. A.22 show the interface ($\phi = 0$). In every case two vortices can be seen. However, the drop is deformed differently. Consider the first type of mesh refinement (figures (a)–(c)). With increasing resolution, the interface widens, and the drop deforms less and shortens in the flow direction. On the other hand, finer drops with thinner interface (figures (d) and (e)) are more deformed compared to the base-case. The internal circulations migrate almost to the tips of the drop (compare figure (c) and (d)). The same remarks refer to other cases at different Pe.

Now consider a higher Ch (with the interface thickness of 2 [lu]). The drop shape and internal circulations are shown in Fig. A.23 at $Pe = 4$ for different mesh refinement types: (a)–(c) constant $Ch = 0.1$ (the first principle); (a), (d), (e) fixed interface width of two lattice units. $Pe = 4$ was chosen because simulations are sta-

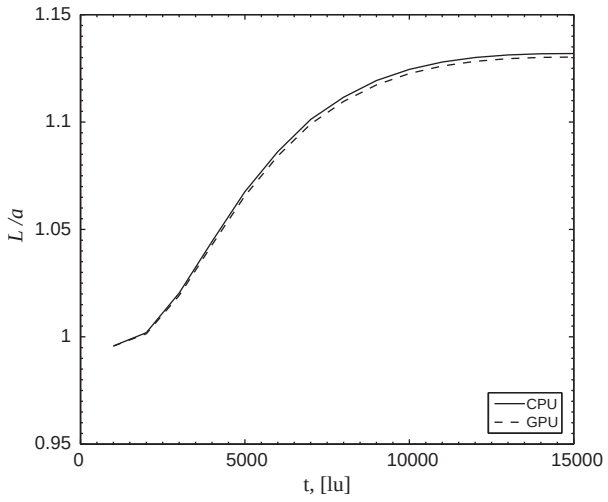

Fig. B.24. Drop elongation L/a change in time obtained using CPU and GPU codes.

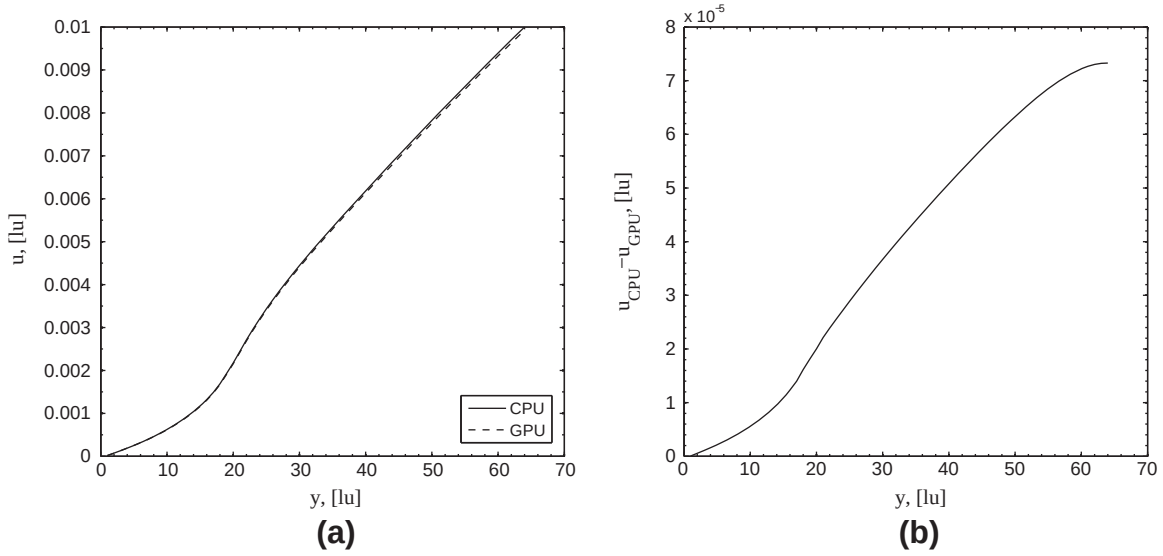

Fig. B.25. The horizontal velocity component u obtained using CPU and GPU codes as a function of vertical coordinate y starting from the drop center and up to the wall (a) and the difference between these two values (b).

ble in the entire range of drop radii. As one can see, none of the mesh refinement simulations with the first principle were able to capture two vortices inside the drop. The interface is so thick relative to the drop diameter that the circulations cannot develop. When the size of the drop was increased while keeping the interface thickness constant, two vortices were captured (figures (d) and (e)). However the intensity of these circulations is different. The finest drop has more developed flow inside.

Appendix B. Comparison of CPU and GPU codes

To compare the results of the CPU and GPU codes, the following simulation was performed: a drop with radius $a = 20$ [lu] in a simulation domain of $6.4a \times 6.4a \times 6.4a$ (full size before symmetry-type boundary conditions) at $\mathrm{Re} = 0.375, \mathrm{Ca} = 0.1, \lambda = 1, Pe = 3.2$, and $Ch = 0.1$. The evolution of drop elongation L/a in time is shown in Fig. B.24. The relative deviation between steady state values is 0.15%. This deviation is attributed to the difference in the velocity fields caused by the use of two different types of velocity boundary conditions. The velocity of the moving wall in the CPU code was set using a procedure proposed by Mussa et al. (2009), and in GPU code the boundary condition of Ladd (1994) was utilized. In the method of Mussa et al. (2009), the wall is located exactly on the last node, while in the method of Ladd (1994) the wall is located one-half grid spacing beyond the last fluid node. This difference is shown in Fig. B.25 where the horizontal velocity component obtained with the two codes is plotted along a line starting from the center of the drop and up to the sheared wall. Since the difference between the elongation of the drop in simulations with the two codes is negligibly small, it is concluded that the CPU and GPU codes produce effectively identical results.

References

Ahmed, N.K., Hecht, M., 2009. A boundary condition with adjustable slip length for lattice Boltzmann simulations. J. Stat. Mech. P09017, 1–14.

Badalassi, V.E., Ceniceros, H.D., Banerjee, S., 2003. Computation of multiphase systems with phase field models. J. Comput. Phys. 190, 371–397.

Bazhlekov, I.B., Anderson, P.D., Meijer, H.E.H., 2004. Nonsingular boundary integral method for deformable drops in viscous flows. Phys. Fluids 16, 1064–1081.

Bentley, B.G., Leal, L.G., 1986. An experimental investigation of drop deformation and breakup in steady, two-dimensional linear flows. J. Fluid Mech. 167, 241–283.

Bhatnagar, P.L., Gross, E.P., Krook, M., 1954. A model for collision processes in gases. I. Small amplitude processes in charged and neutral one-component systems. Phys. Rev. 94, 511–525.

Cahn, J.W., Hilliard, J.E., 1958. Free energy of a nonuniform system. I. Interfacial free energy. J. Chem. Phys. 28, 258–267.

Cahn, J.W., Hilliard, J.E., 1959. Free energy of a nonuniform system. III. Nucleation in a two-component incompressible fluid. J. Chem. Phys. 31, 688–699.

Cristini, V., Renardy, Y., 2006. Scalings for droplet sizes in shear-driven breakup: non-microfluidic ways to monodisperse emulsions. FDMP 2, 77–93.

Cristini, V., Guido, S., Alfani, A., Bławzdziewicz, J.B., Loewenberg, M., 2003. Drop breakup and fragment size distribution in shear flow. J. Rheol. 47, 1283–1298.

Davies, J.T., 1987. A physical interpretation of drop sizes in homogenizers and agitated tanks, including the dispersion of viscous oils. Chem. Eng. Sci. 42, 1671–1676.

De Groot, S.R., Mazur, P., editors, 1984. Non-equilibrium Thermodynamics. Dover Publications.

Ding, H., Spelt, P.D.M., Shu, C., 2007. Diffuse interface model for incompressible two-phase flows with large density ratios. J. Comput. Phys. 226, 2078–2095.

Jacqmin, D., 1999. Calculation of two-phase Navier–Stokes flows using phase-field modeling. J. Comput. Phys. 155, 96–127.

Jacqmin, D., 2000. Contact-line dynamics of a diffuse fluid interface. J. Fluid Mech. 402, 57–88.

Janssen, P.J.A., Anderson, P.D., 2007. Boundary-integral method for drop deformation between parallel plates. Phys. Fluids 19, 043602.

Kendon, V.M., Cates, M.E., Pagonabarraga, I., Desplat, J.-C., Bladon, P., 2001. Inertial effects in three-dimensional spinodal decomposition of a symmetric binary fluid mixture: a lattice Boltzmann study. J. Fluid Mech. 440, 147–203.

Kennedy, M.R., Pozrikidis, C., Skalak, R., 1994. Motion and deformation of liquid drops, and the rheology of dilute emulsions in simple shear flow. Comput. Fluids 23, 251–278.

Khismatullin, D.B., Renardy, Y., Cristini, V., 2003. Inertia-induced breakup of highly viscous drops subjected to simple shear. Phys. Fluids 15, 1351–1354.

Komrakova, A.E., Derksen, J.J., Eskin, D., in press. Simulations of dispersion formation in liquid-liquid turbulent flows. In: 8th International Conference on Multiphase Flow, ICMF 2013, Jeju, Korea, May 26–31.

Kusumaatmaja, H., 2008. Lattice Boltzmann Studies of Wetting and Spreading on Patterned Surfaces. Ph.D. Thesis, University of Oxford.

Kwak, S., Pozrikidis, C., 1998. Adaptive triangulation of evolving, closed, or open surfaces by the advancing-front method. J. Comput. Phys. 145, 61–68.

Ladd, A.J.C., 1994. Numerical simulations of particulate suspensions via a discretized Boltzmann equation Part I. Theoretical Foundation. J. Fluid Mech. 271, 285–309.

Li, J., Renardy, Y.Y., Renardy, M., 2000. Numerical simulation of breakup of a viscous drop in simple shear flow through a volume-of-fluid method. Phys. Fluids 12, 269–282.

Magaletti, F., Picano, F., Chinappi, M., Marino, L., Casciola, C.M., 2013. The sharp-interface limit of the Cahn–Hilliard/Navier–Stokes model for binary fluids. J. Fluid Mech. 714, 95–126.

Marks, C.R., 1998. Drop Breakup and Deformation in Sudden onset Strong Flows. Ph.D. Thesis, University of Maryland.

Mason, T.G., Bibette, J., 1997. Shear rupturing of droplets in complex fluids. Langmuir 13, 4600–4613.

Mussa, A., Asinari, P., Luo, L.-S., 2009. Lattice Boltzmann simulations of 2D laminar flows past two tandem cylinders. J. Comput. Phys. 228, 983–999.

Penrose, O., Fife, P.C., 1990. Thermodynamically consistent models of phase-field type for the kinetics of phase transitions. Physica D 43, 44–62.
Pope, S.B., 2000. Turbulent Flows. Cambridge University Press.
Pozrikidis, C., 1992. Boundary Integral and Singularity Methods for Linearized Viscous Flow. Cambridge University Press.
Rallison, J.M., 1981. A numerical study of the deformation and burst of a viscous drop in general shear flows. J. Fluid Mech. 109, 465–482.
Rallison, J.M., 1984. The deformation of small viscous drops and bubbles in shear flows. Ann. Rev. Fluid Mech. 16, 45–66.
Renardy, Y.Y., Cristini, V., 2001a. Effect of inertia on drop breakup under shear. Phys. Fluids 13, 7–13.
Renardy, Y.Y., Cristini, V., 2001b. Scalings for fragments produced from drop breakup in shear flow with inertia. Phys. Fluids 13, 2161–2164.
Renardy, Y.Y., Cristini, V., Li, J., 2002. Drop fragment distributions under shear with inertia. Int. J. Multiphase Flow 28, 1125–1147.
Shan, X., Chen, H., 1993. Lattice Boltzmann model for simulating flows with multiple phases and components. Phys. Rev. E 47, 1815–1819.
Shardt, Orest, Derksen, J.J., Mitra, Sushanta K., 2013. Simulations of droplet coalescence in simple shear flow. Langmuir. http://dx.doi.org/10.1021/la304919p.
Stone, H.A., 1994. Dynamics of drop deformation and breakup in viscous fluids. Ann. Rev. Fluid Mech. 26, 65–102.
Swift, M.R., Orlandini, E., Osborn, W.R., Yeomans, J.M., 1996. Lattice Boltzmann simulations of liquid–gas and binary fluid systems. Phys. Rev. E 54, 5041–5052.
Taylor, G.I., 1932. The viscosity of a fluid containing small drops of another fluid. Proc. Roy. Soc. Lond. A 138, 41–48.
Taylor, G.I., 1934. The formation of emulsions in definable fields of flow. Proc. Roy. Soc. Lond. A 146, 501–523.
Van der Sman, R.G.M., van der Graaf, S., 2008. Emulsion droplet deformation and breakup with Lattice Boltzmann model. Comput. Phys. Commun. 178, 492–504.
Xi, H., Duncan, C., 1999. Lattice Boltzmann simulations of three-dimensional single droplet deformation and breakup under simple shear flow. Phys. Rev. E 59, 3022–3037.
Yue, P., Feng, J.J., Liu, C., Shen, J., 2004. A diffuse-interface method for simulating two-phase flows of complex fluids. J. Fluid Mech. 515, 293–317.
Yue, P., Zhou, C., Feng, J.J., 2010. Sharp-interface limit of the Cahn–Hilliard model for moving contact lines. J. Fluid Mech. 645, 279–294.
Zhao, X., 2007. Drop breakup in dilute newtonian emulsions in simple shear flow: new drop breakup mechanisms. J. Rheol. 51, 367–392.